

# Computational and Experimental Analysis of Mach 5 Air Flow over a Cylinder with a Nanosecond Pulse Discharge

Nicholas J. Bisek,<sup>\*</sup> Jonathan Poggie<sup>†</sup>

*Air Force Research Laboratory, Wright-Patterson AFB, OH, 45433-7512, USA*

and

Munetake Nishihara<sup>‡</sup> Igor Adamovich,<sup>§</sup>

*The Ohio State University, Columbus, OH 43210, USA*

A computational study is performed for Mach 5 air flow over a cylinder with a dielectric barrier discharge actuator set into the cylinder surface. The actuator is pulsed at nanosecond time scales, which rapidly adds energy to the flow, thereby creating a shock wave that travels away from the pulse source. As the shock wave travels upstream, it interacts with the standing bow-shock and momentarily increases the bow-shock standoff distance. This phenomenon is also observed in phase-locked schlieren photography captured during the experiment. The focus of this paper is to reproduce flow phenomena observed in the experiment using high-fidelity computations in order to provide additional insight into the shock-shock interaction, the effect the dielectric barrier discharge pulse has on the surface properties of the cylinder, and develop a reduced-order phenomenological model representative of the nanosecond pulse discharge system. Experimental and high-fidelity modeling studies of the nanosecond pulse dielectric barrier discharge plasma actuators are known to operate with relatively low temperatures. This work explores the possibility that the induced compression wave is generated by rapid thermalization of the discharge which results in a local temperature rise occurring on longer time scales. Two-dimensional simulations are performed and provide many useful details about the discharge event while comparing with many measurements captured by the experiment. However, the simulations indicate the experiment experiences significant three-dimensional effects, thus requiring a three-dimensional simulation of the entire experiment to accurately capture the complex cylinder/tunnel-sidewall interaction and replicate the resultant flow. Three-dimensional results of the discharge event reveal the discharge pulse produces a compression wave that interacts with the standing bow-shock and that the momentary increase in the bow-shock standoff distance is not due to the interaction the three-dimensional compression wave has with the cylinder/tunnel-sidewall boundary layer.

## Nomenclature

|           |   |
|-----------|---|
| $a, b, c$ | = equatorial radii of an ellipsoid, [m]   |
| $c_p$     | = coefficient of pressure, $\frac{p-p_\infty}{\frac{1}{2} \rho_\infty u^2}$     |
| $c_h$     | = nondimensional heating coefficient, $\frac{q_w}{\frac{1}{2} \rho_\infty u^3}$ |
| $M$       | = Mach number   |
| $p$       | = pressure, [Pa]  |
| $R$       | = gas constant, [J/kg-K]  |
| $q$       | = heat flux, [W/m <sup>2</sup> ]  |

<sup>\*</sup>Research Aerospace Engineer, High-Speed Flow Research Group, Computational Aerophysics Branch. Member AIAA.

<sup>†</sup>Team Lead, High-Speed Flow Research Group, Computational Aerophysics Branch. Associate Fellow AIAA.

<sup>‡</sup>Postdoctoral Researcher, Nonequilibrium Thermodynamics Laboratories, Dept. of Mechanical Engineering, Member AIAA.

<sup>§</sup>Professor, Nonequilibrium Thermodynamics Laboratories, Dept. of Mechanical Engineering, Associate Fellow AIAA.

| Report Documentation Page  |                                    |                                     | Form Approved<br>OMB No. 0704-0188                        |   |                                 |
|--|------------------------------------|-------------------------------------|---|---|---------------------------------|
| Public reporting burden for the collection of information is estimated to average 1 hour per response, including the time for reviewing instructions, searching existing data sources, gathering and maintaining the data needed, and completing and reviewing the collection of information. Send comments regarding this burden estimate or any other aspect of this collection of information, including suggestions for reducing this burden, to Washington Headquarters Services, Directorate for Information Operations and Reports, 1215 Jefferson Davis Highway, Suite 1204, Arlington VA 22202-4302. Respondents should be aware that notwithstanding any other provision of law, no person shall be subject to a penalty for failing to comply with a collection of information if it does not display a currently valid OMB control number. |                                    |                                     |   |   |                                 |
| 1. REPORT DATE<br><b>JAN 2012</b>  |                                    | 2. REPORT TYPE                      |   | 3. DATES COVERED<br><b>00-00-2012 to 00-00-2012</b> |                                 |
| 4. TITLE AND SUBTITLE<br><b>Computational and Experimental Analysis of Mach 5 Air Flow over a Cylinder with a Nanosecond Pulse Discharge</b>   |                                    |                                     |   | 5a. CONTRACT NUMBER                                 |                                 |
|  |                                    |                                     |   | 5b. GRANT NUMBER                                    |                                 |
|  |                                    |                                     |   | 5c. PROGRAM ELEMENT NUMBER                          |                                 |
| 6. AUTHOR(S)   |                                    |                                     |   | 5d. PROJECT NUMBER                                  |                                 |
|  |                                    |                                     |   | 5e. TASK NUMBER                                     |                                 |
|  |                                    |                                     |   | 5f. WORK UNIT NUMBER                                |                                 |
| 7. PERFORMING ORGANIZATION NAME(S) AND ADDRESS(ES)<br><b>Air Force Research Laboratory, Wright-Patterson AFB, OH, 45433-7512</b>   |                                    |                                     |   | 8. PERFORMING ORGANIZATION REPORT NUMBER            |                                 |
| 9. SPONSORING/MONITORING AGENCY NAME(S) AND ADDRESS(ES)  |                                    |                                     |   | 10. SPONSOR/MONITOR'S ACRONYM(S)                    |                                 |
|  |                                    |                                     |   | 11. SPONSOR/MONITOR'S REPORT NUMBER(S)              |                                 |
| 12. DISTRIBUTION/AVAILABILITY STATEMENT<br><b>Approved for public release; distribution unlimited</b>  |                                    |                                     |   |   |                                 |
| 13. SUPPLEMENTARY NOTES  |                                    |                                     |   |   |                                 |
| 14. ABSTRACT   |                                    |                                     |   |   |                                 |
| 15. SUBJECT TERMS  |                                    |                                     |   |   |                                 |
| 16. SECURITY CLASSIFICATION OF:  |                                    |                                     | 17. LIMITATION OF ABSTRACT<br><b>Same as Report (SAR)</b> | 18. NUMBER OF PAGES<br><b>30</b>                    | 19a. NAME OF RESPONSIBLE PERSON |
| a. REPORT<br><b>unclassified</b>   | b. ABSTRACT<br><b>unclassified</b> | c. THIS PAGE<br><b>unclassified</b> |   |   |                                 |

|               |  |
|---------------|--|
| $Q$           | = total energy input by actuator, [W]  |
| $T$           | = temperature, [K]   |
| $u, v, w$     | = streamwise, transverse, and spanwise velocity components, [m/s]                      |
| $U$           | = velocity magnitude, [m/s]  |
| $x, y, z$     | = streamwise, transverse, and spanwise coordinates                                     |
| $\alpha$      | = accommodation coefficient for partial slip wall boundary conditions                  |
| $\gamma$      | = specific heat ratio, (1.4 for air)   |
| $\varepsilon$ | = emissivity   |
| $\theta$      | = angle along cylinder surface, $\tan^{-1} \left( \frac{y-y_{cy}}{x-x_{cy}} \right)$   |
| $\lambda$     | = mean free-path, $\frac{\mu}{\rho} \sqrt{\frac{\pi}{2R T}}$ , [m]                     |
| $\mu$         | = kinetic viscosity, [kg/m-s]  |
| $\rho$        | = density, [kg/m <sup>3</sup> ]  |
| $\sigma_0$    | = Stefan-Boltzmann constant, $5.6704 \cdot 10^{-8}$ J/m <sup>2</sup> -s-K <sup>4</sup> |
| $\tau$        | = duration of the energy deposition pulse, [s]   |

#### Subscript

|          |                                   |
|----------|-----------------------------------|
| $c$      | = center of ellipsoid             |
| $cy$     | = center of the cylinder          |
| $g$      | = gas                             |
| $ve$     | = vibrational-electron-electronic |
| $w$      | = wall                            |
| $0$      | = stagnation                      |
| $\infty$ | = freestream                      |

## I. Introduction

A recent experimental study of a nanosecond pulse Dielectric Barrier Discharge (DBD) in a Mach 5 flow demonstrated the feasibility of plasma-based supersonic flow control.<sup>1</sup> A bow-shock perturbation on a microsecond time scale was detected in phase-locked schlieren visualization. Compression wave generation due to a rapid localized heating from the DBD propagates upstream from the cylinder surface and interacts with the standing bow-shock. This interaction temporarily increases the shock standoff distance. This series of events can be repeated at time spacing up to 10  $\mu$ s (100 kHz). Previous demonstration of the nanosecond pulse DBD includes separated flow reattachment<sup>2</sup> up to Mach = 0.85, characterization of compression wave propagation in a quiescent air,<sup>3</sup> and visualization of large-scale, spanwise vortex over the airfoil<sup>4</sup> at M = 0.3.

The flow control mechanism (rapid heating) in these experiments<sup>2,4</sup> appears consistent with a Localized Arc Filament Plasma Actuator (LAFPA).<sup>5-7</sup> The main idea of this approach is forcing the flow with a high amplitude, high bandwidth perturbation, at a frequency approaching one of the flow instability frequencies, thereby triggering subsequent growth. Previous flow-control studies using LAFPA actuators in atmospheric pressure jet flows<sup>5-7</sup> (M = 0.9-2.0), demonstrated significant localized heating and repetitive shock-wave formation by the plasma, large-scale coherent structure generation, and mixing enhancement. This effect was achieved at a low actuator power ( $\sim 10$  W per actuator), at forcing frequencies near the jet column instability frequency (preferred mode). This low power budget contrasts with previous bow shock control studies, typically on the order of 10 kW, using pulsed DC discharge,<sup>8</sup> pulsed microwave discharge,<sup>9</sup> and laser optical breakdown.<sup>10,11</sup>

In this paper, the demonstrated effect will be reproduced using the LeMANS code,<sup>12,13</sup> developed at University of Michigan.<sup>14,15</sup> LeMANS was previously used for hypersonic flow-control by energy deposition,<sup>12</sup> therefore rapid energy coupling by the nanosecond pulse DBD is modeled in the same phenomenological approach. It is assumed that the phenomenological model prediction replicates the thermal effect of the DBD. Various important parameters, such as temperature distribution, pressure and heat coefficients are not available in the experiment. Thus, this modeling study is meant to reveal details about the flow perturbation mechanism, and afford an evaluation of its validity for practical applications, such as flow control at hypersonic inlet, isolator, and engine exhaust, while concurrent work by Poggie *et al.*<sup>16</sup> focuses on high-fidelity modeling of only the dielectric barrier discharge in order to identify the relevant energy transfer processes and develop a reduced-order model of the DBD.

The nonequilibrium plasma wind tunnel used in the experiment was initially manufactured to study

nonequilibrium hypersonic flows and develop optical diagnostics that can be portable to and perform measurements at national ground hypersonic test facilities. Owing to this purpose, the freestream velocity and temperature have been measured. Results from previous measurements of the freestream velocity and temperature are used for freestream uncertainty quantification.

The work uses LeMANS to compute flow around a 5 mm cylinder and a 6 mm cylinder using two-dimensional computations to compare with existing experiments. While the 5 mm cylinder simulation results match the experiment, the 6 mm cylinder simulation results over-predict the bow-shock location. The nanosecond DBD experiment used the 6 mm cylinder, so a parametric study exploring the uncertainties associated with the freestream, wall boundary, and thermo-chemical nonequilibrium flow conditions is conducted to quantify their effects on the standing bow-shock location. The study revealed that none of the parameters explained the discrepancy in bow-shock location. Nonetheless, the two-dimensional simulations allow the large design-space to be explored with minimal computational cost, including results from the phenomenological energy deposition modeling of the discharge event. The energy deposition modeling results are able to replicate the DBD discharge induced compression wave speed and resultant perturbed bow-shock shape and qualitatively match phase-locked schlieren images.

In order to explain the bow-shock standoff discrepancy, a three-dimensional computation of the full tunnel is computed and found to agree well with all available experimental measurements. The results show that cylinder/tunnel sidewall interaction produces a significant pressure drop along the cylinder span, which draws the standing bow-shock closer to the cylinder. In addition, a three-dimensional simulation with the phenomenological energy deposition model representing the discharge event is able to reproduce many of the features observed in the phase-locked schlieren images of the experiment.

## II. Experimental Facilities

A schematic of a small-scale Mach 5 nonequilibrium wind tunnel is shown in Fig. 1 (also used in Ref. 17, 18). The wind tunnel was operated using dry air supplied from high-pressure cylinders, at plenum pressures of  $p_0 = 370$  Torr (0.5 atm), and the mass flow rate of 7 g/s. The steady state run time at the constant static pressure in the supersonic test section is up to 10 seconds. The flow expands through an aerodynamically contoured Mach 5 nozzle, with the throat height of 1.6 mm. Top and bottom walls of the supersonic test section after the nozzle exit each diverge at a  $1.5^\circ$  angle to provide boundary layer relief. Rectangular optical access windows, made of UV-grade fused silica, are flush mounted in all four walls in the supersonic test section, providing ample optical access for schlieren photography, emission spectroscopy, Planar Laser Induced Fluorescence (PLIF) visualization / thermometry,<sup>17,18</sup> and NO<sub>2</sub> Molecular Tagging Velocimetry (MTV)<sup>19</sup> diagnostics, as well as currently on-going vibrational temperature measurement by picosecond Coherent Anti-Stokes Raman Scattering (CARS) system.<sup>20</sup>

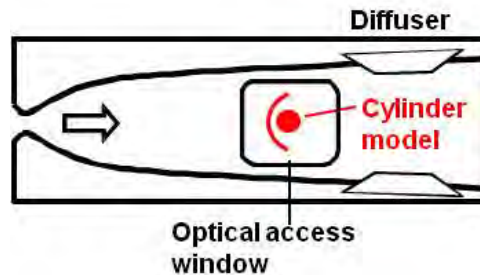


**Figure 1. Schematic of the Mach 5 wind tunnel with a cylinder model installed in the test section.**

The dimensions of a quartz cylinder model used to generate a bow-shock and also used as a DBD actuator is 4 cm long, 6 mm outer diameter, and 4 mm inner diameter. The model is located 14.5 cm downstream of the throat (3.5 cm downstream of the end of nozzle contour), where the flow cross sectional area is 4 cm x 4.6 cm. The ends of the model are embedded in the optical access windows in the side walls of the test section. The baseline shock standoff distance (without nanosecond pulse discharge), measured in the schlieren photography is 1.2 mm, with the spanwise length of about 1 cm, which is 25% of the test section width. The spanwise extent of the bow-shock is limited by the boundary layer growth on the sidewalls of the test section.<sup>17</sup>

The test section static pressure,  $p_\infty = 1.2$  Torr (160 Pa), was measured using a wall pressure tap in the side wall at the end of the nozzle, and 4 cm upstream of the cylinder model. The pressure is assumed to be constant through the sidewall boundary, a valid assumption for a laminar boundary layer (no experimental measurements taken thus far have indicated the wall boundary layer is turbulent). The flow Mach number inferred from the plenum pressure and freestream static pressure is  $M_\infty = 4.6$ , while the total pressure measured at the flow stagnation point (downstream of the bow-shock) was  $p = 36$  Torr, which corresponds to a freestream Mach number of  $M_\infty = 4.8$ , using one-dimensional normal shock relations and assuming the static pressure is constant across the side-wall boundary layer.

Figure 2 shows a cartoon of the electrode configuration for the bow-shock perturbation by the nanosecond pulse DBD. One actuator electrode is composed of a 1 cm long, 3 mm diameter copper tube with a tube wall thickness of 0.35 mm, and is immersed inside the quartz tube. Since the tube's inside diameter is 4 mm, the actuator electrode is positioned to contact the quartz surface near the upstream side, as seen in Fig. 9. The other electrode consists of a strip of adhesive copper tape 1.5 mm wide and 12 mm long, attached to the outside surface of the quartz tube model. The two electrodes overlap over a spanwise distance of 10 mm, centered behind the core flow bow-shock, with the ends of the tape covered by non-conducting Kapton® tape. Output pulse voltage and current were measured during each run. Measured peak voltage and current are 27 kV and 70 A, respectively, coupling between 4-7 mJ/pulse.

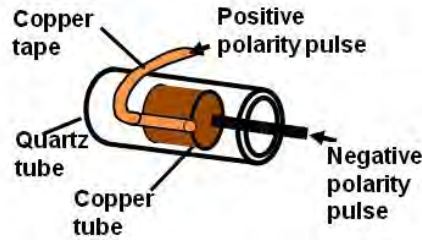


**Figure 2. Diagram of the cylinder model with a nanosecond pulse surface DBD plasma actuator.**

Time evolution of the shock generated by the NanoSecond Dielectric Barrier Discharge (NSDBD), as well as its interaction with the bow shock was recorded using a phase-locked schlieren system.<sup>3</sup> It was shown that a discharge pulse generates a compression wave that propagates upstream and locally ‘pushes’ the bow-shock away from the cylinder. This perturbed region bends away from the flow stagnation line, convects downstream, and eventually returns the shock envelop to the baseline shock shape about 20  $\mu$ s later. Image sets for this microsecond-scale shock-shock interaction were taken both for a ‘single pulse’ mode (pulse repetition rate of 200 Hz), and ‘double pulse’ mode (two pulses separated by a 10 microsecond delay, which corresponds to a pulse repetition rate of 100 kHz). This study will primarily use on the ‘single pulse’ mode, so each discharge pulse acts on the baseline bow-shock. Additional details about the NSDBD process are available in Ref. 1.

### A. Freestream flow parameters

The facility is able to achieve Mach 5 flows using a blow-down wind tunnel. While it is not possible to exactly characterize the test section for each experiment run, through various proven approaches, the inputs necessary for a computational simulation can be determined. As shown in previous work,<sup>17</sup> the test section has an inviscid core that composes about 25% of the cross-section area. Since the cylinder test model is essentially two-dimensional and only composes a fraction of the core flow, it is reasonable to assume that the freestream flow is uniform and the resultant flow-field will be two-dimensional. This assumption is justified by looking at Fig. 3, a top-down view of phase-locked schlieren image at  $p_0 = 370$  Torr dry air (baseline condition), with the standoff distance  $\Delta S = 1.2$  mm.

Freestream velocity was measured  $u_\infty = 719 \pm 6$  m/s in the NO<sub>2</sub> MTV.<sup>19</sup> In this measurement, a small amount of NO<sub>2</sub> ( $\sim 1\%$  mole fraction), was seeded in the main nitrogen flow at the plenum pressure,  $p_0 = 370$  Torr. A pulse-burst laser system<sup>21</sup> generated two simultaneous outputs: one for the photo-dissociation of NO<sub>2</sub> into NO and O at 355 nm to tag a line in the flow, the other tuned at 226 nm for interrogation of the line progression by NO PLIF imaging. The NO fluorescence intensity distributions were fitted by a Gaussian curve, and it was found that the average velocity is 719 m/s with absolute statistical error of  $\sigma = 5.8$  m/s.

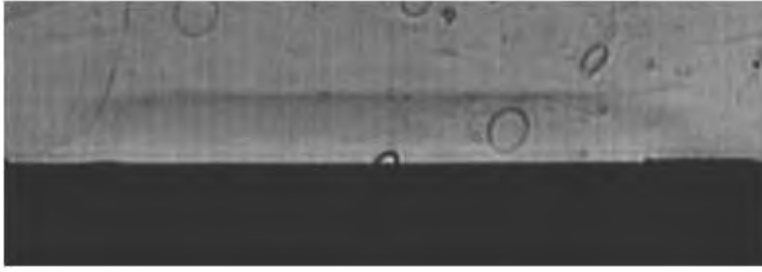


**Figure 3.** Phase-locked schlieren image (top-down view) in dry air at  $p_0 = 370$  Torr at baseline condition (without discharge). Flow direction is top to bottom in the figure.

The NO PLIF thermometry was used for temperature measurement behind the Mach 5 bow-shock in Ref. 18. A sheet of laser was tuned to pump a rotational transition of  $J = 5.5$  or  $J = 16.5$  on the  $\text{NO}(X, v' = 0 \rightarrow A, v'' = 0)$  band. The pair of these lines was selected because the ratio of absorption strength is linear at around  $T_0 = 300$  K. In one of preliminary experiments, sheet laser wavelengths were tuned to excite the  $J = 5.5$  and  $J = 9.5$  rotational states in order to probe lower temperatures in the freestream. Only a few of experiments have been carried out thus far with some uncertainty in the results. But, the results tend to fall within a temperature range of about  $T_\infty = 50\text{--}60$  K, which appears consistent with a freestream temperature obtained by considering the freestream pressure ratio,  $T_\infty = 56$  K. Freestream temperatures calculated from the isentropic relation, using the freestream velocity measured in the  $\text{NO}_2$  MTV measurement, are  $T_\infty = 78$  K, 60 K, and 50 K for Mach numbers of  $M = 4, 4.55$ , and 5, respectively. The freestream temperature for  $M = 4.55$  is also close to this isentropic flow temperature.

As previously mentioned, the test section static pressure,  $p_\infty = 1.2$  Torr (160 Pa), was measured using a wall pressure tap in the side wall at the end of the nozzle, and 4 cm upstream of the cylinder model. The precision on the pressure gauge is 0.1 Torr, so its uncertainty is  $\pm 0.05$  Torr ( $\pm 6.67$  Pa). The freestream density is inferred using the ideal gas relation ( $p = \rho R T$ ). For this work, the freestream dry air is composed of 78% nitrogen ( $\text{N}_2$ ), and 22% oxygen ( $\text{O}_2$ ), by density. Table 1 lists the nominal freestream conditions and uncertainty bounds. The effect of the uncertainties will be addressed in a later section.

**Table 1.** Freestream conditions and uncertainty bounds for Mach 5 air flow around a cylinder.

| Parameter                            | Value                 |
|--------------------------------------|-----------------------|
| $u_\infty$ , [m/s]                   | $719 \pm 6$           |
| $T_\infty$ , [K]                     | $56 \pm 5$            |
| $\rho_\infty$ , [kg/m <sup>3</sup> ] | $0.009924 \pm 0.0013$ |
| $p_\infty$ , [Pa]                    | $160 \pm 6.7$         |
| $M_\infty$                           | $4.76 \pm 0.25$       |

### III. Numerical Method

Flow-field results are obtained using Computational Fluid Dynamics (CFD) to solve the Navier-Stokes equations. The CFD computations are executed using the Michigan Aerothermodynamic Navier-Stokes (LeMANS), code developed at the University of Michigan.<sup>14,15</sup> LeMANS is a general 2D/axisymmetric/3D, parallel, unstructured finite-volume CFD code and has been used previously in numerous studies of hypersonic flows.<sup>12–15</sup> LeMANS may be employed with any of three thermodynamic models: perfect gas, equilibrium, and nonequilibrium thermochemistry. LeMANS employs a two-temperature model to account for thermal nonequilibrium and a standard finite-rate chemistry model for nonequilibrium chemistry. The two temperature model assumes that a single temperature,  $T$ , accounts for the translational and rotational energy modes of all species while the vibrational and electronic energy modes are accounted for by a separate temperature,  $T_{ve}$ . The simulations are performed using second-order accurate spatial discretization and carry double precision arithmetic throughout.

LeMANS is primarily used for steady-state simulations, but is capable of computing time accurate scenarios with first-order temporal accuracy. However, numerical error associated the low temporal accuracy is minimized by enforcing a sub-nanosecond time step ( $\Delta t \leq 1$  ns).

The nanosecond DBD discharge used in the experiment is effectively a thermal actuator. As such, a phenomenological model of dissipative heating is used to represent it. This model is accounted for in the Navier-Stokes equations by the addition of a source term,  $S$ , to the right side of total energy equation,

without any energy being directly deposited into the vibrational-electron-electric energy equation when the simulation is performed assuming thermodynamic nonequilibrium. Deposition of all the energy into the translational mode is a strong assumption, but is adequate for the purpose of this study since it is assumed the compression wave generated by the DBD is due to a rapid transfer of energy into the translation energy mode, an observation seen in previous work by Popov.<sup>22</sup>

The shape and location of the actuator are modeled with contours of constant  $S$  having an ellipsoidal shape. This approach has been used successfully in previous numerical investigations.<sup>12</sup> The strength (total energy), deposited into the flow uses exponential decay from the centroid of the energy deposition pattern, which for two-dimensional simulations is:

$$S = \frac{Q}{\pi a b} \exp \left( - \left( \frac{\hat{x}}{a} \right)^2 - \left( \frac{\hat{y}}{b} \right)^2 \right) \quad (1)$$

$$\hat{x} = (x - x_c)$$

$$\hat{y} = (y - y_c)$$

where variables  $a$  and  $b$  are the equatorial radii (along the  $x$  and  $y$  axes). Coordinates  $(x_c, y_c)$  represent the centroid of the ellipsoid. Note that  $Q$  represents the total power deposited in the flow and  $\iint_{-\infty}^{\infty} S dx dy = Q$ .

### A. Grid Independence

Figure 4 shows a structured mesh for a two-dimensional computational domain around a 6 mm diameter cylinder. Flow direction is left to right, and the stagnation point is located at  $x = 0.003$  m. Only the first  $90^\circ$  of the cylinder surface is computed in this section to minimize computational cost and because measurements behind the cylinder, such as the wake or shear layer structure, were not captured in the experiment. Note full cylinder computations are discussed in subsequent sections. The meshes were developed such that clustering in the radial direction occurs at both the cylinder surface and at the bow-shock, while the mesh in the azimuthal direction is distributed to provide orthogonality of the cells at the bow-shock.

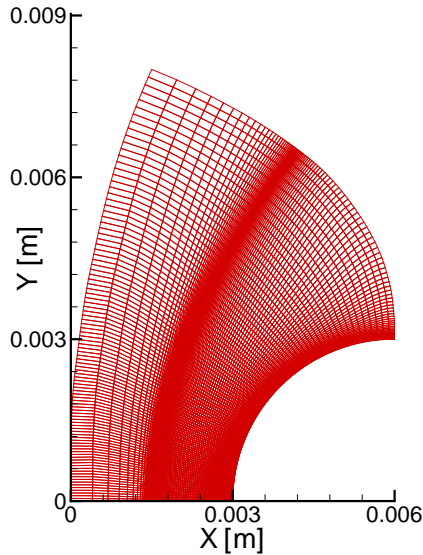


**Figure 4. Shock-fitted grid for Mach 5 air flow around a cylinder. ( $100 \times 100$ )**

Three doubly refined grids:  $50 \times 50$  (coarse),  $100 \times 100$  (medium), and  $200 \times 200$  (fine), were used for the grid independence study. Input parameters were taken from the nominal conditions listed in Table 1;  $u_\infty = 719$  m/s,  $T_\infty = 56$  K, and  $\rho_\infty = 0.009924$  kg/m<sup>3</sup>. Since the input parameters correspond to the baseline scenario (i.e., steady-state), the solution is advanced until the root-mean-square residual error approaches machine-precision and remains unchanged for subsequent time steps, as seen in Fig. 5. As the mesh number increases, the number of iterations required for the convergence also increases due to the reduction in the time step required to maintain stability, which is calculated based on the smallest cells

size used in the computational domain. In addition, a maximum time step of  $\Delta t = 1 \text{ } \mu\text{s}$  is enforced for all steady-state simulations performed in this paper.

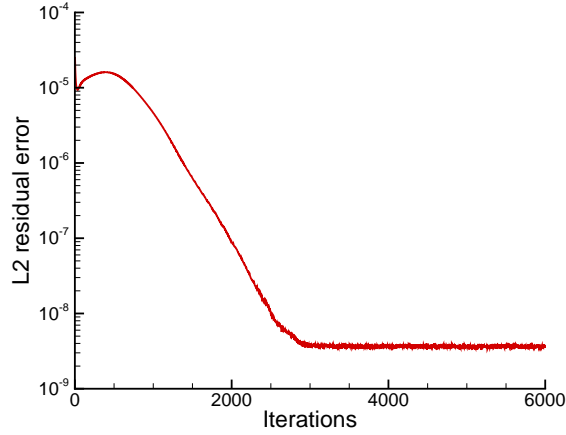


**Figure 5. Root-mean-square residual error for the nominal baseline case with the medium grid.**

Figure 6 compares the temperature contours from the fine grid (top) and medium grid (bottom). The distributions are nearly identical, except at the bow-shock, where the shock appears more smeared for the medium grid. While the shock thickness decreases with increasing mesh number, the standoff distance (defined as the distance between the stagnation point and the location of maximum density gradient), remains the same ( $\Delta S = 1.55 \text{ mm}$ ), for all three grids.

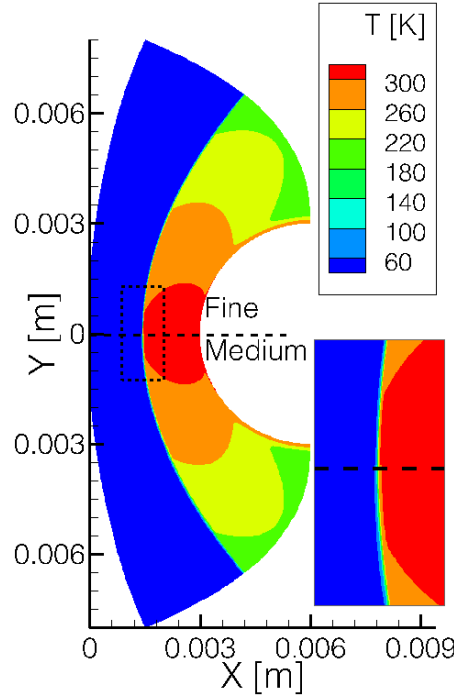


**Figure 6. Temperature contours for Mach 5 air flow over a cylinder with fine grid (top) and medium grid (bottom).**

Figure 7 plots pressure coefficient,  $c_p$ , and nondimensional heating coefficient,  $c_h$ , along the cylinder surface for all three grids. Coordinates along the cylinder are converted into the degree angle,  $\theta$ , with  $\theta = 0^\circ$  located at the stagnation point. The pressure coefficient is nearly identical for all three grids, while the nondimensional heating coefficient exhibits an offset for the coarse grid. Both the pressure and



nondimensional heating coefficients achieved on the fine grid replicate those from the medium grid. Therefore, the medium grid ( $100 \times 100$ ), is considered grid-independent and will be used in the remaining two-dimensional baseline simulations, unless otherwise noted.

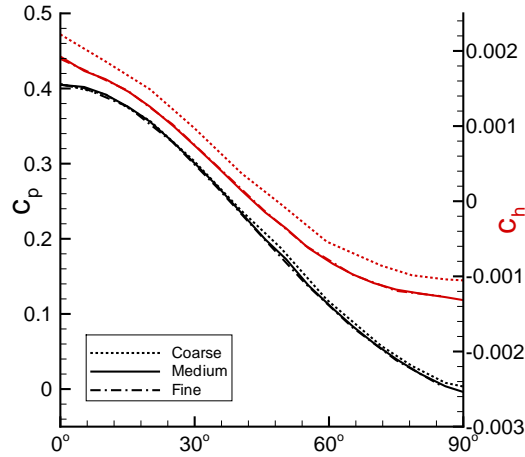


**Figure 7. Pressure and nondimensional heat coefficient along the cylinder surface for various grids.**

The temperature distribution is compared with a schlieren image of a bow-shock ahead of 6 mm diameter cylinder in Fig. 8(a). The experiment's bow-shock standoff distance of  $\Delta S = 1.2$  mm is 20% smaller than the computed standoff distance of  $\Delta S = 1.55$  mm. Also displayed in the figure is an empirical relation for the shock envelop developed by Billig *et al.*,<sup>23,24</sup> which was developed by comparing schlieren images from many shock tube experiments and has dependencies on Mach number and cylinder radius. Billig's empirical relationship to determine the bow-shock standoff location on the stagnation line is specified later in Eq. (3). For a Mach number of  $M = 4.8$  and the radius of 3 mm, Billig's empirical standoff distance  $\Delta S = 1.42$  mm is much closer to the LeMANS computed standoff distance and shows a good agreement with the shock profile as well.

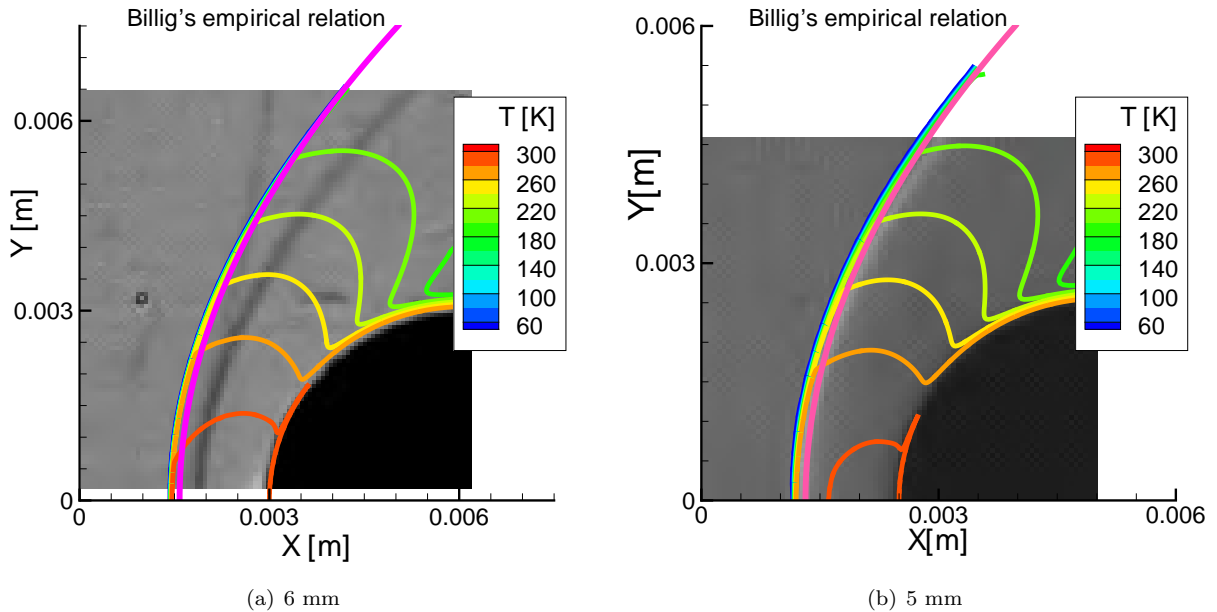


**Figure 8. Contour lines of temperature for Mach 5 air flow over a cylinder for two cylinder diameters. The figures include schlieren images from the experiment and Billig's empirical formula of the shock envelope.<sup>24</sup>**

The discrepancy in the bow-shock standoff location between the computation and the experiment suggests there may be inappropriate assumptions made in the simulation or there are three-dimensional effects in the experiment that cannot be replicated by the two-dimensional computation. To help assess the validity of the two-dimensional computational results, a computation was performed for a 5 mm diameter cylinder scenario, which was also performed experimentally (although the nanosecond DBD was not employed for this experimental setup). As seen in Fig. 8(b), the 5 mm cylinder experimental results are in much better agreement with the computations and Billig’s empirical relationship. These results suggest that the differences in standoff distance observed in the 6 mm diameter cylinder scenario are mostly likely attributed to a three-dimensional effect found in the experiment or greater uncertainty in freestream and wall boundary conditions. The following subsections explore the effects associated with tunnel and boundary conditions using the two-dimensional simulations since exploration of the full three-dimensional simulation requires a significant increase in computational cost.

## B. Wall Boundary Conditions

One uncertainty about the experiment is the temperature of the cylinder surface. Since the cylinder is initially at room temperature, one assumption is that the cylinder surface is at a constant isothermal condition. However, given the experiment’s long run time (10 seconds), the cylinder should cool to adiabatic conditions (i.e., no heat transfer to the surface). Another common approach in CFD is to assume the surface is in radiative equilibrium. This assumption is modeled by using the Stefan-Boltzmann Law:

$$q_w = \varepsilon \sigma_0 T_w^4 \quad (2)$$

where  $q_w$  is the heat transfer to the wall,  $\varepsilon$  is the emissivity of the body, and  $\sigma_0$  is the Stefan-Boltzmann constant. Assuming the body (i.e., cylinder surface), can be treated as a ‘black body’, its emissivity is unity ( $\varepsilon = 1$ ). However, Fig. 9 shows the cylinder is composed of quartz (a dielectric), which has an emissivity<sup>25</sup> of  $\varepsilon = 0.93$ , except for the exposed electrode, which has an emissivity<sup>26</sup> of  $\varepsilon = 0.02$ . Preliminary simulations accounting for the actual thickness of the exposed electrode (0.1 mm), extruded from the quartz surface did not significantly alter the resultant flow-field, so the remaining simulations assume the cylinder surface has a continuous radius of 3 mm (i.e., the exposed electrode is incorporated into the cylinder surface). Table 2 tabulates the four scenarios considered for the wall boundary condition study. Each steady-state scenario uses the shock-fitted grid-independent mesh and nominal freestream conditions listed in Table 1, without the nanosecond discharge event (i.e., baseline scenario).

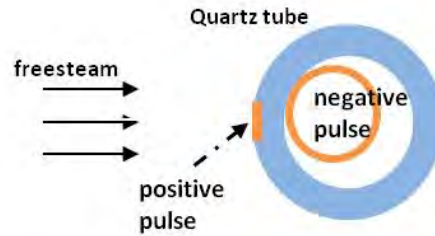
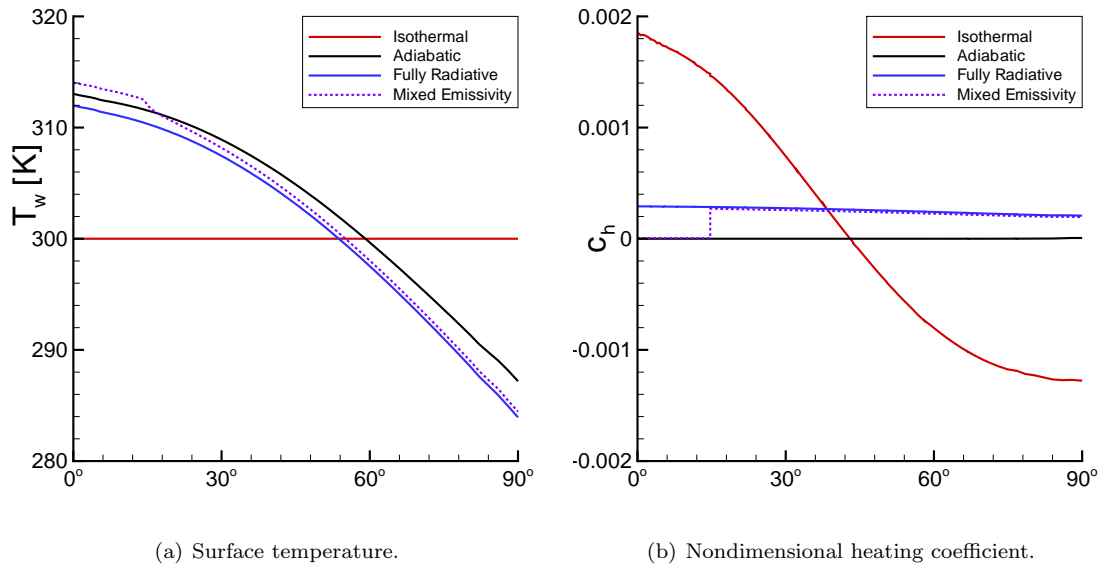


Figure 9. Side-view cartoon of the experimental setup of the cylinder.

Table 2. Wall boundary condition scenarios investigated for Mach 5 air flow over a cylinder.

| Scenario         | Details  |
|------------------|--|
| Adiabatic        | $q_w = 0$  |
| Isothermal       | $T_w = 300 \text{ K}$  |
| Fully Radiative  | $\varepsilon = 1$  |
| Mixed Emissivity | $\varepsilon_{\text{quartz}} = 0.93$<br>$\varepsilon_{\text{copper}} = 0.02$ |

Figures 10(a) and 10(b) show the surface temperature distribution and the nondimensional heating coefficient, along the surface for each of the scenarios. As seen in Fig. 10(a), the adiabatic solution is very similar to the radiative boundary condition scenarios, whereas the nondimensional heating coefficient is very similar for the isothermal and radiative boundary conditions.



**Figure 10. Distributions along the surface of a cylinder in Mach 5 air with various wall boundary conditions.**

Table 3 tabulates the shock standoff distance, which is determined by identifying the peak density gradient in streamwise direction (i.e., along the  $x$ -axis). While the surface profiles seen in Figs. 10(a) and 10(b) exhibit differences, the shock standoff distance is not influenced by the wall boundary condition selected. This occurs because the boundary layer that develops on the cylinder surface is quite small, and since the adiabatic wall boundary condition only significantly influences the boundary layer thickness, the shock standoff distance is not influenced by the boundary condition enforced. The effect of wall boundary conditions is expected to be more pronounced at higher temperatures, such as during the nanosecond discharge event, where the gas temperature near the stagnation point reaches 2000 K on a microsecond time scale.

**Table 3. Shock standoff distance for various wall boundary scenarios.**

| Scenario         | Shock Standoff |
|------------------|----------------|
| Adiabatic        | 1.55 mm        |
| Isothermal       | 1.55 mm        |
| Fully Radiative  | 1.55 mm        |
| Mixed Emissivity | 1.55 mm        |

### C. Thermo-Chemical Nonequilibrium

The freestream conditions are quite cold (see Table 1). As such, it is unlikely that a significant amount of thermal-chemical nonequilibrium is present in the flow. For completeness, with regards to chemical nonequilibrium, simulations were run using a one-species perfect gas, and a five-species gas ( $N_2$ ,  $O_2$ ,  $NO$ ,  $N$ , and  $O$ ), using Park's 1990 data sets. Since the latter of the two scenarios requires LeMANS to carry 5 conservation equations for the mass, the computational resources required to obtain a solution also increases. As anticipated, the simulation results show no appreciable differences between the one-species perfect gas and the five-species finite-rate chemistry simulations. For completeness, two simulations are also conducted allowing for thermal nonequilibrium of the vibrational temperature. The Landau-Teller model<sup>27</sup> is used to account for energy exchange between the vibrational-electronic and the translational-rotational energy modes.

Typically, rates of vibration-translation energy transfer in a nitrogen-oxygen system are very low,<sup>28</sup> and therefore vibrational temperature at the plenum  $T_{ve}=300$  K is assumed frozen in the freestream. For this thermo-chemical nonequilibrium case, translational and vibrational temperature distributions are compared in Fig. 11(a). For comparison, Fig. 11(b) displays translational and vibrational temperature distributions

at the freestream vibrational temperature,  $T_{ve}=240$  K, which corresponds to a scenario where thermal equilibrium exists up to the nozzle throat, at which point it freezes and remains frozen downstream into the test section.

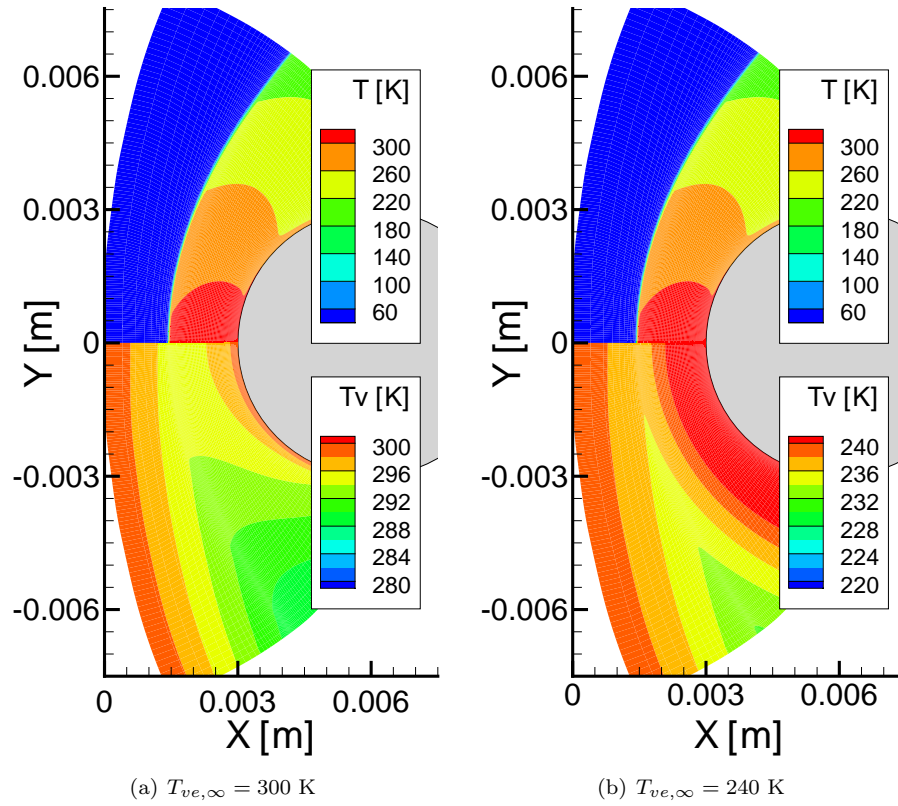


**Figure 11. Translational and vibrational temperature contours for Mach 5 air flow over a 6mm cylinder.**

As seen in the figures, the vibrational temperatures are essentially frozen across the shock. Also, no noticeable differences in the standoff distance or wall properties are observed in either scenario. Therefore, the thermal nonequilibrium effects are ignored for the remainder of the baseline calculations. However, finite-rate chemistry is included in the energy deposition scenarios due to the rapid rise in local temperature during the discharge event.

#### D. Freestream Uncertainty Quantification

The freestream conditions observed in the wind tunnel have uncertainty associated with them. As such, it is important to quantify the effect these uncertainties have of flow properties of interest, such as standoff distance, as they may explain the discrepancy observed for the 6 mm diameter scenario. LeMANS requires the freestream density, temperature, and velocity as input parameters. These three variables determine the possible scenarios that need to be simulated to quantify the uncertainty in baseline shock standoff distance associated with the nominal freestream conditions. Table 4 lists the various runs with the parameter combinations. The simulations were performed assuming thermal-chemical equilibrium and the isothermal wall boundary condition,  $T_w = 300$  K.

Results of standoff distance are summarized in Fig. 12, which plots standoff distance versus Mach number. The points are denoted by color to indicate the Reynolds number (based on cylinder radius). As seen in the figure, the standoff distance decreases with increasing Reynolds number. The general trend of these points appears to be consistent with Billig's empirical formula for cylinder flow.<sup>24</sup>

$$\frac{\Delta S}{r} = 0.386 \exp\left(\frac{4.67}{M^2}\right) \quad (3)$$

Table 4. Input parameters for uncertainty quantification of freestream conditions for Mach 5 air flow over a cylinder.

| Run | $u_\infty$ , [m/s] | $T_\infty$ , [K] | $\rho_\infty$ , [kg/m <sup>3</sup> ] | $Re_\infty/L$ [m <sup>-1</sup> ] | Mach |
|-----|--------------------|------------------|--------------------------------------|----------------------------------|------|
| 1   | 713                | 50               | 0.008876                             | $1.97 \cdot 10^6$                | 5.02 |
| 2   | 713                | 50               | 0.011578                             | $2.57 \cdot 10^6$                | 5.02 |
| 3   | 713                | 60               | 0.008876                             | $1.59 \cdot 10^6$                | 4.59 |
| 4   | 713                | 60               | 0.011578                             | $2.07 \cdot 10^6$                | 4.59 |
| 5   | 725                | 50               | 0.008876                             | $2.0 \cdot 10^6$                 | 5.11 |
| 6   | 725                | 50               | 0.011578                             | $2.61 \cdot 10^6$                | 5.11 |
| 7   | 725                | 60               | 0.008876                             | $1.62 \cdot 10^6$                | 4.66 |
| 8   | 725                | 60               | 0.011578                             | $2.11 \cdot 10^6$                | 4.66 |

where  $\Delta S$  is the shock standoff distance,  $r$  is the cylinder radius, and  $M$  is the upstream Mach number. The similarity between Eq. (3) and the solutions in Fig. 12 exists because expansion of Eq. (3) generates the quadratic dependence of the standoff distance over a small range of Mach numbers, while the quadratic curve fit for the solution points in Fig. 12 yields a similar dependence on the Mach number,  $\Delta S$  [mm] =  $0.103 M^2 - 1.151 M + 4.688$ .

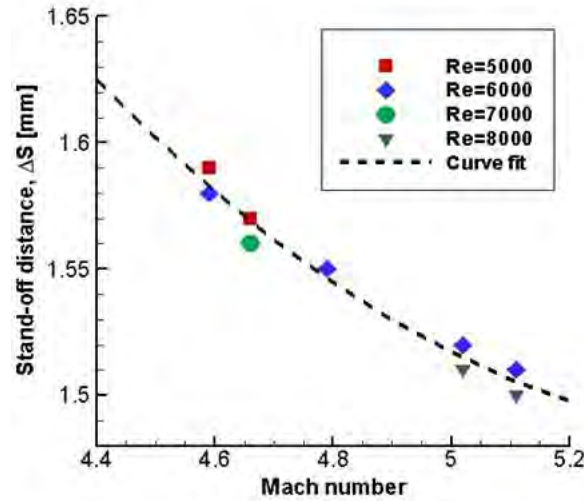


Figure 12. Standoff distance versus Mach number for various scenarios of air flow over a 6 mm cylinder.

Comparing the maximum and minimum computed standoff distances to the nominal scenario shows the uncertainty in standoff distance due to uncertainty in freestream conditions is  $\pm 3\%$ , which is essentially negligible for the energy deposition scenario since the maximum standoff distance increase was 25%.<sup>1</sup> As such, the nominal freestream conditions listed in Table 1 are employed for the remaining two-dimensional simulations.

## E. Partial Slip Walls

Since the experiment was performed in a very cold, low pressure wind tunnel, it is possible that part of the cylinder experiences velocity slip along its surface due to the transition of flow into to the free molecular regime. To check for partial velocity slip, the gradient length Knudsen number developed by Boyd *et al.*,<sup>29</sup> is computed from the nominal baseline steady-state solution using Eq. (4):

$$Kn_{GL} = \frac{\lambda}{Q} \left| \frac{\partial Q}{\partial l} \right| \quad (4)$$

where  $\lambda$  is the mean free-path,  $Q$  is any primitive quantity ( $U$ ,  $T$ ,  $p$ , or  $\rho$ ), and the derivative is taken in the direction of the maximum gradient. Note when computing the velocity magnitude Knudsen number gradient, the gradient is normalized by the local velocity magnitude, except when the velocity is zero. During these situations, the gradient is normalized by the local speed of sound. The Navier-Stokes equations breakdown when the flow transitions from continuum to free molecular flow, which is assumed when  $\text{Kn}_{\text{GL}} > 0.05$ .<sup>30</sup> However, using partial slip wall boundary conditions where  $\text{Kn}_{\text{GL}} > 0.05$  will extend the range of validity of the Navier-Stokes solver being employed.

Figure 13 shows contours for the gradient length Knudsen number for the nominal baseline scenario (using the grid shown in Fig. 25). As seen in Fig. 13, the flow experiences continuum breakdown in the vicinity of the shock and along the top and leeward side of the cylinder. Continuum breakdown within the shock is anticipated due to the strong flow discontinuity, though breakdown of the governing equations in this region does not adversely affect the post-shock flow conditions because the Rankine-Hugoniot condition is preserved through the shock. However, continuum breakdown observed on the cylinder surface is problematic as it indicates that the LeMANS solver should not be used in that region without modifying the surface boundary conditions to account for the slight deviation from the continuum assumption made when deriving the Navier-Stokes equations used in LeMANS.

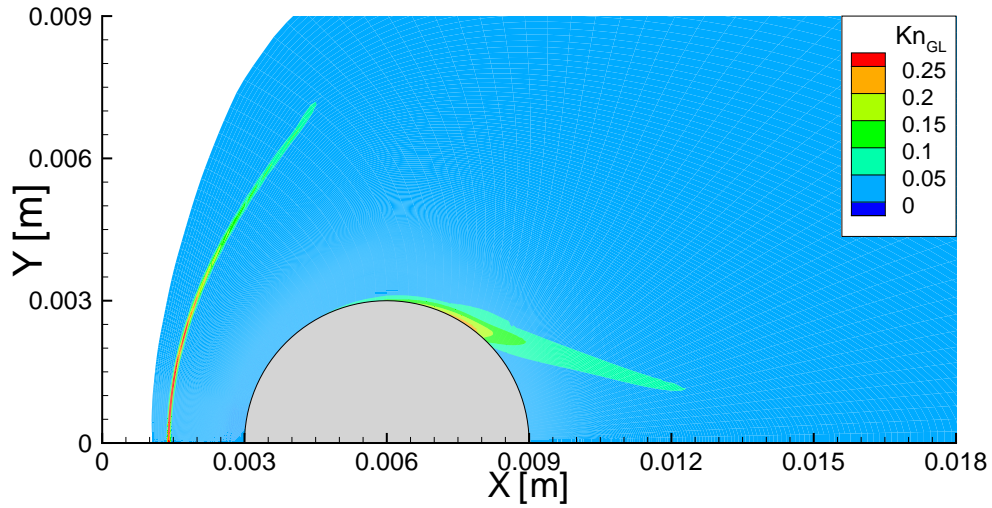


**Figure 13.** Contours of the gradient length Knudsen number for Mach 5 air flow over a cylinder.

In order to quantify the effects of continuum breakdown on the shock structure, a partial slip wall model is employed using Maxwell's slip condition, as described in Refs. 30,31. Maxwell's slip condition was derived for a flat plate. It modifies the surface's tangential velocity, and, subsequently, provides a temperature jump. Equations (5) and (6) show the modifications to the surface velocity and temperature:

$$U_w = A \left( \frac{2 - \alpha}{\alpha} \right) \lambda \left. \frac{\partial u_x}{\partial n} \right|_n \quad (5)$$

$$T_w = T_g - \left( \frac{2 - \alpha}{\alpha} \right) \lambda \left. \frac{\partial T}{\partial n} \right|_n \quad (6)$$

where  $\lambda$  is the mean free-path,  $T_w - T_g$  is the temperature jump,  $\alpha$  is the accommodation coefficient, and  $A$  is a constant based on the scenario being considered. For simplicity in this work, both  $A$  and  $\alpha$  are set to unity, as it is unclear what they should be for a good nonequilibrium solution for the flow considered. The derivative is computed normal to the wall surface and  $u_x$  is the velocity in the streamwise direction (along the wall surface).

In order to validate the partial slip boundary used, a nonequilibrium solution is computed using the Direct Simulation Monte Carlo (DSMC), code: HAP, developed by Burt *et al.*<sup>32</sup> Figure 14 shows the surface velocity and temperature jump for both the DSMC and LeMANS with Maxwell's slip condition. While the DSMC solution exhibits a large amount of scatter (due to a minimal sample of particles used in the simulation and an insufficient number of samples collected to further reduce the variance), the solution



confirms that the flow experiences surface velocity slip and a small temperature jump as the flow moves over the top and along the leeward side of the cylinder. In addition, the DSMC results provide direction for the proper adjustments to  $A$  and  $\alpha$  in the partial slip boundary conditions. However, the values selected provide reasonable adjustments to the wall boundary conditions and are considered sufficient to quantify the effect a partial slip wall has on the bow-shock location.

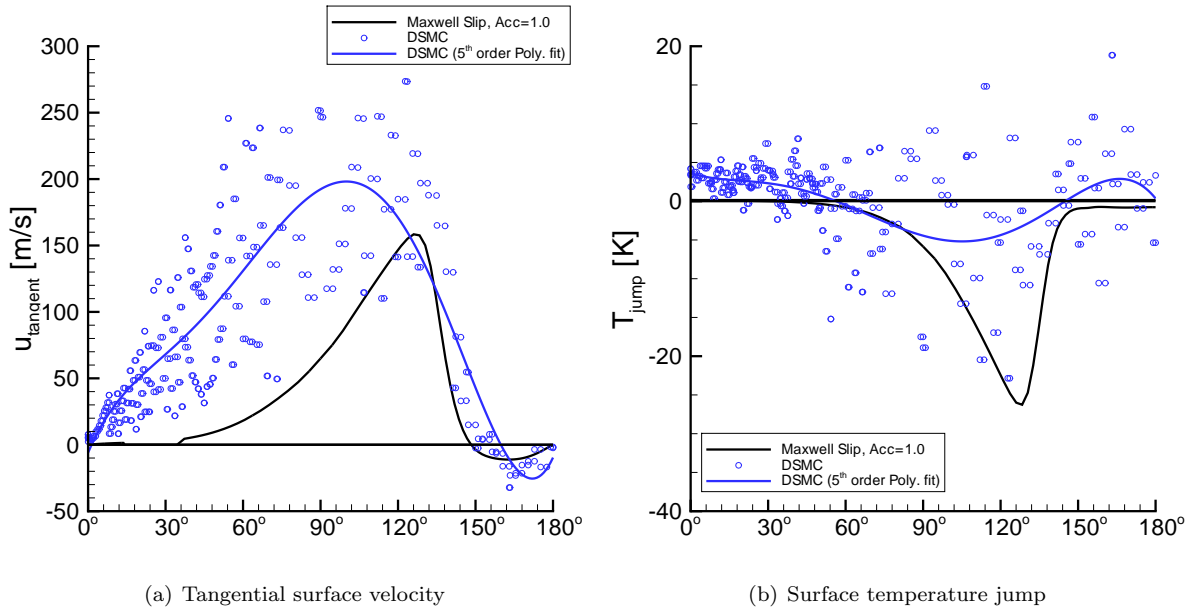


**Figure 14. Surface properties for Mach 5 air flow over a cylinder from a DSMC simulation and LeMANS using a simple Maxwell wall slip condition.**

While the surface does experience partial velocity slip, which changes the size and flow properties of the recirculating wake region, the bow-shock standoff is not influenced by the change in wall boundary conditions, as seen in Fig. 15. As such, continuum breakdown along the top and leeward side of the cylinder does not explain the observed discrepancy in bow-shock standoff distance and is neglected in the remaining simulations.

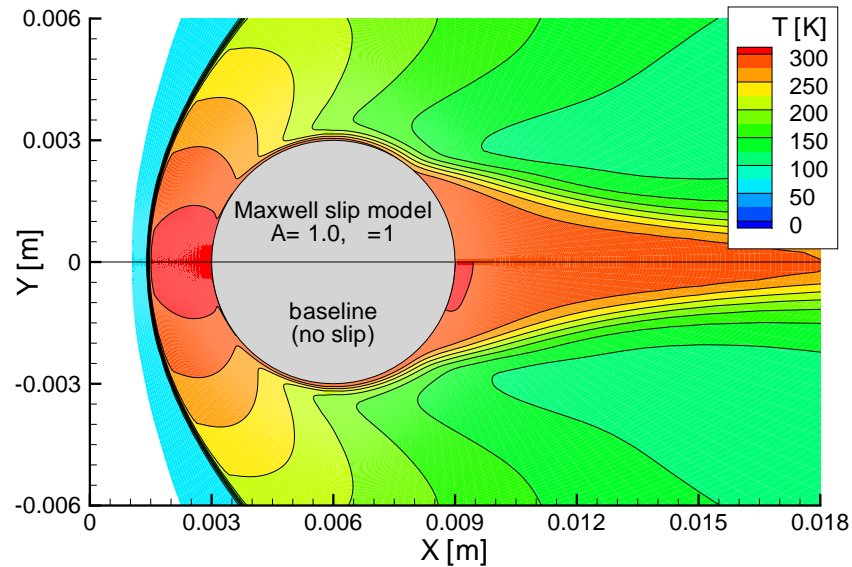


**Figure 15. Temperature contours for Mach 5 air flow over a cylinder with and without partial velocity slip and temperature jump wall boundary condition.**

As seen in the previous subsections, uncertainty in the computed shock standoff distance due to freestream conditions, boundary conditions, and thermochemical effects is relatively small and does not account for the discrepancy in shock standoff seen in the experiment. While the difference in shock standoff distance in the baseline flow is important for replicating and quantifying the effects of the discharge event, the next section uses the two-dimensional approach to qualitatively explore the nanosecond DBD discharge effect and subsequent perturbation on the flow. These computations are performed to develop sufficient grid and time-step bounds for the discharge simulations, and to develop and optimize the shape of the deposition model before transitioning to three-dimensional simulations.

#### IV. 2D Energy Deposition

The nanosecond DBD event performed in the experiment results in rapid thermalization of the electrical energy in the surrounding air, which produces a compression wave that interacts with the cylinder bow-shock. Since the thermal efficiency of the DBD is not exactly known, one of the critical parameters in the reduced-order model used in the CFD modeling of event is the rate of energy thermalization, which is controlled by the parameter  $Q$  in Eq. (1).

Figure 16 shows a grid used in the energy deposition simulation. The grid points are spaced uniformly both in the  $x$  and  $\theta$  directions to reduce the spatial error due to the propagation of the bow-shock perturbed by the compression wave formed during the discharge event. Three doubly refined grids have been used to study the effect of grid resolution on the numerical solution,  $201 \times 101$  points (coarse),  $401 \times 201$  points (medium) and  $801 \times 401$  points (fine). For the coarse grid, the cell size is  $1 \cdot 10^{-5} \text{ m} \times 2.3 \cdot 10^{-5} \text{ m}$ . The computational domain length in the streamwise direction extends 2 mm from the stagnation point of the cylinder (see Fig. 16), which allows the shock standoff distance to increase by up to 30% from the steady-state baseline solution standoff distance without being influenced by the domain inlet.

The spatial profile of energy deposition by the discharge used in the calculations is set in Eq. (1). The size of the energy deposition region was determined from the size of the plasma visible emission in the experiment, and approximated as an ellipse with axes of  $a = 0.1 \text{ mm}$  and  $b = 0.3 \text{ mm}$ , with the center of the ellipse located at the stagnation point (for the coordinate system used in the computations  $x_c = 3.0 \text{ mm}$  and  $y_c = 0.0 \text{ mm}$ ), and Gaussian distribution of power density. Thus, approximately 67% of the input power is deposited for  $x \leq a$  and  $y \leq b$ , and 95% of power is deposited for  $x \leq 2a$  and  $y \leq 2b$ . The temporal profile of energy deposition is modeled as a step function. Due to the difference between baseline shock standoff distance predicted by the CFD model and the experimental value ( $\Delta S = 1.55 \text{ mm}$  versus  $\Delta S = 1.2 \text{ mm}$ ), obtaining agreement with all experimentally measured parameters, i.e. compression wave speed of  $U_c = 370 \text{ m/s}$ , perturbed bow-shock propagation velocity of  $U_s = 92 \text{ m/s}$ , and shock standoff distance increase of 25%, is problematic. Since the compression wave is expanding radially as it travels, its strength decreases significantly with distance traveled before interacting with the bow-shock. As a result, a stronger wave will need to be generated in the computational exercise in order to produce a perturbed bow-shock with dynamics similar to those observed in the experiment.

To ensure spatial and temporal independence during the discharge event and subsequent flow interaction, simulations were conducted using an energy deposition pulse  $\tau = 800 \text{ ns}$  long, with total power deposited  $Q = 3 \text{ kW}$ , and a fixed computational time step  $\Delta t = 0.5 \text{ ns}$ . These parameters were selected for the grid independence study because the deposition energy represents a high thermal efficiency scenario and the resultant flow perturbation is significant.

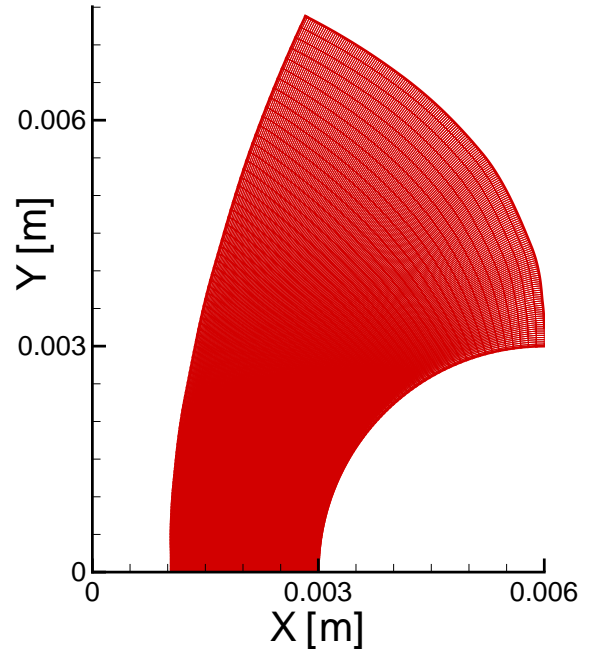
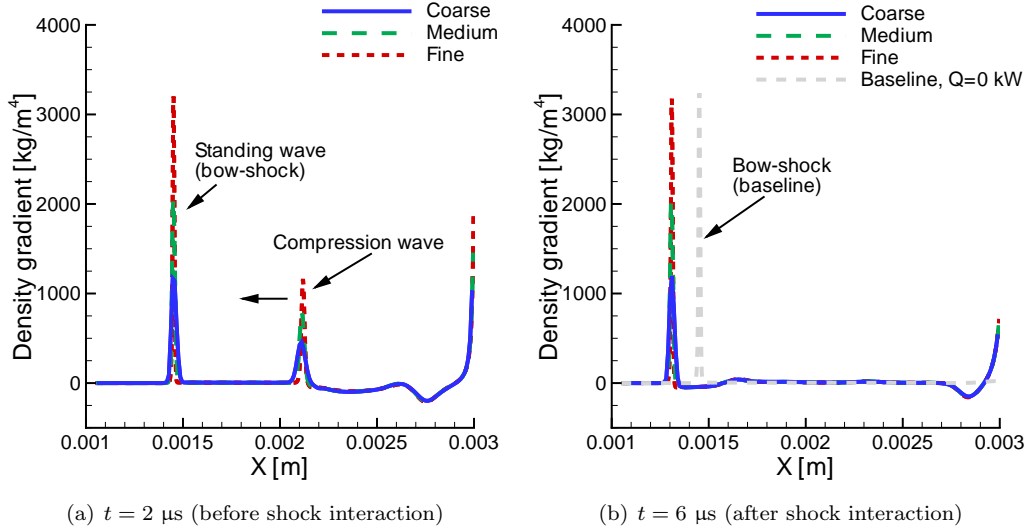


Figure 16. Grid used for the energy deposition simulation ( $201 \times 101$ ).

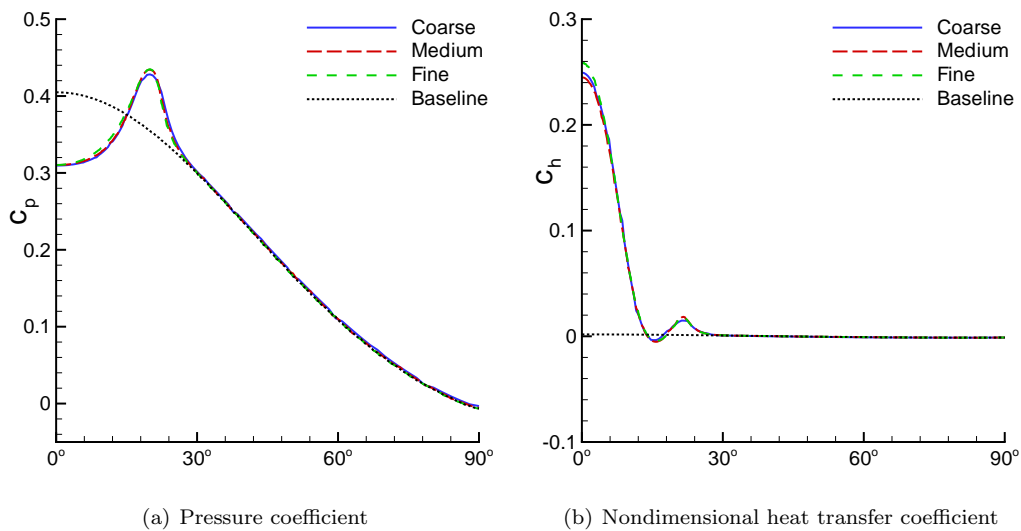


Figure 17(a) plots density gradient distributions at  $t = 2 \mu\text{s}$  after the beginning of the energy deposition pulse, obtained using three different grids and a time step of  $\Delta t = 0.5 \text{ ns}$ . The density gradient was calculated using a 3-point central difference. The bow-shock and the propagating compression wave front are located at  $x = 0.00145 \text{ m}$  and  $x = 0.0021 \text{ m}$ , respectively. It can be seen that the magnitude of the density gradient increases approximately linearly with increasing grid resolution. Similarly, the magnitude of the peak density gradient is also observed in Fig. 17(b), which shows density gradient distributions of the perturbed bow-shock at  $t = 6 \mu\text{s}$  after the beginning of the energy deposition pulse. These results indicate that the medium grid has sufficient resolution to adequately capture the discharge event and resultant shock-shock interaction.



**Figure 17.** Density gradient distributions for the perturbed bow-shock obtained using three different grids at various times after the energy deposition pulse. Flow direction is left to right.

Figures 18(a) and 18(b) show distributions of wall pressure and nondimensional heat transfer coefficients on the cylinder model at  $t = 2 \mu\text{s}$  after the discharge pulse, calculated for the three different grids. It can be seen that with pulsed energy deposition, peak wall pressure is reached off stagnation line, approximately at  $\theta = 20^\circ$  (see Fig. 18(a)). Pulse energy deposition also results in significant heat transfer increase near the stagnation line (see Fig. 18(b)). These results indicate that all three grids provide sufficient resolution to obtain accurate estimates of the cylinder surface properties.



**Figure 18.** Surface distributions at  $t = 2 \mu\text{s}$  after energy deposition pulse for various grids.

Figure 19 plots compression wave speed and perturbed bow-shock velocity from simulations for three fixed time steps:  $\Delta t = 5$  ns, 1 ns, and 0.5 ns on the three different grids. To calculate the compression wave speed, the location of the density peak was sampled every 400 ns at  $t = 1 - 3$   $\mu$ s after the beginning of the energy deposition pulse. After the compression wave reached the standing bow-shock (approximately 4  $\mu$ s after the beginning of the energy deposition pulse), the location of the density peak was sampled every 400 ns at  $t = 4 - 6$   $\mu$ s after the beginning of the energy deposition pulse to determine the perturbed bow-shock speed. From Fig. 19, it can be seen that the calculated compression wave speed and perturbed bow-shock speed depend on grid resolution when the computation time step is  $\Delta t = 5$  ns, but fully converges when the time step is reduced to  $\Delta t = 0.5$  ns. Based on these results, a fixed time step of  $\Delta t = 0.5$  ns and the medium grid ( $401 \times 201$ ), provide sufficient temporal and spatial independence and is used for all subsequent two-dimensional simulations.

Figure 20 shows dependence of compression wave propagation velocity on deposited pulse energy for input powers of  $Q = 1, 2$ , and 3 kW. Since the energy is deposited uniformly in time, the duration of energy deposition pulse is varied as follows:  $400\text{ns} \leq \tau \leq 3200$  ns for  $Q = 1$  kW,  $200\text{ns} \leq \tau \leq 1600$  ns for  $Q = 2$  kW, and  $200\text{ns} \leq \tau \leq 1200$  ns for  $Q = 3$  kW, respectively. Fig. 20 also denotes the speed of sound evaluated using the post-shock temperature averaged along the stagnation line ( $T = 307$  K,  $C_s = 351$  m/s).

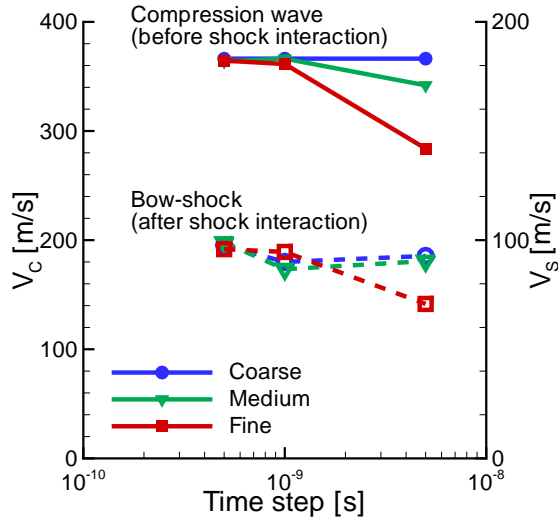


Figure 19. Compression wave propagation velocity (closed symbols) and perturbed bow-shock velocity (open symbols) vs. time step for the three grids used.

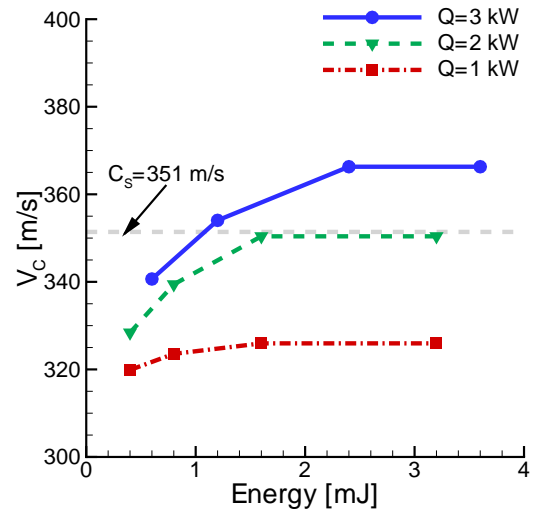


Figure 20. Compression wave speed dependence on input power and energy added (i.e. duration of energy deposition pulse).

As seen in Fig. 20, input power of  $Q = 1$  kW and 2 kW produce a compression wave speed that increases with total pulse energy until an energy of 1.6 mJ, whereas the input power of  $Q = 3$  kW achieves a compression wave speed that increases up to pulse energy 2.4 mJ. This is due to the fact that the smaller values of  $Q$  fail to produce a supersonic compression wave, which limits the amount of energy that can be used to increase the wave speed. Since the compression wave is supersonic in the experiment (see Fig. 21), a value of  $Q \geq 3$  kW seems most appropriate to investigate the discharge effect and subsequent flow perturbation. In addition, selection of an input power of  $Q = 3$  kW for  $\tau = 800$  ns, corresponds to a pulse energy of 2.4 mJ, which is consistent with about 30% the experiment's coupled pulse energy 'quickly' thermalizing. The thermal efficiency assumed here is consistent with a study by Popov.<sup>22</sup>

Figure 22(a) shows density distributions along the stagnation streamline, calculated for pulse duration of  $\tau = 1200$  ns ( $Q = 3$  kW), at  $t = 200$  ns, 400 ns, 800 ns, and 1200 ns after the beginning of the energy deposition. As seen in the figure, the region of fluid displacement (i.e. density reduction near the stagnation point) expands up to  $t = 800$  ns, which results in density increase to the left of the energy deposition region. At  $t \geq 800$  ns, the density in the energy deposition region no longer decreases, thus limiting mass displacement due to energy deposition and, consequently, compression wave speed. After this limit is reached, additional energy input no longer contributes to increasing the compression wave speed. As a result, the compression wave speed remains constant for pulse deposition durations greater than 800 ns (for  $Q = 3$  kW).

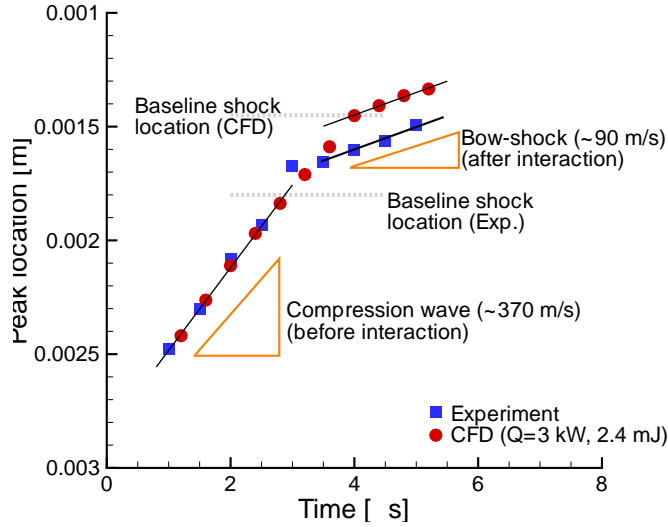


Figure 21. Comparison of predicted peak density gradient location with the experiment (phase-locked schlieren). ( $401 \times 201$ ,  $\Delta t = 0.5$  ns,  $Q = 3$  kW,  $\tau = 800$  ns)

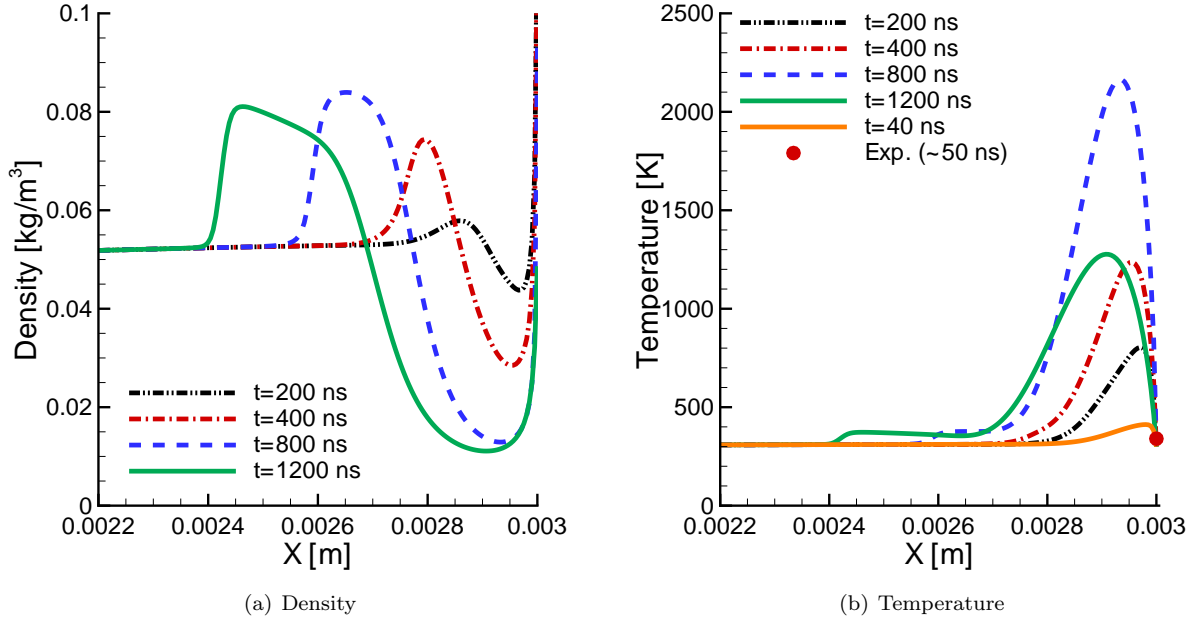


Figure 22. Stagnation streamline distributions at different delays after the start of the energy deposition pulse ( $Q = 3$  kW,  $\tau = 800$  ns), for Mach 5 air over a cylinder.

Using a total input power of  $Q = 3$  kW and energy deposition pulse duration of  $\tau = 800$  ns yields the maximum compression wave speed for its total input power while providing a wave speed that is slightly greater than the experiment's measured wave speed. As such, this scenario provides the best agreement for both compression wave velocity and perturbed bow-shock propagation velocity along the stagnation line, as shown in Fig. 21. The total energy deposited for this scenario amounts to 2.4 mJ/pulse (for the full geometry), which means the nanosecond DBD pulse would have to have a thermal efficiency of over 30%. However this conclusion can be confusing since the baseline bow-shock location is 1.55 mm from the cylinder in the computation and only 1.2 mm for the experiment. Since the shock is located farther from the cylinder, the energy deposited in the simulation must be exaggerated in order to create a compression wave with sufficient speed and strength such that its interaction with the standing bow-shock produces a

resultant combined wave that has the same velocity as the experiment.

Figure 22(b) plots temperature distributions at the same delays as Fig. 22(a). In these calculations, temperature at the stagnation point is fixed at  $T = 300$  K (isothermal wall). However, the peak temperature increases during the energy deposition process and reaches maximum at  $t = 800$  ns,  $T = 2160$  K. This peak temperature value is much higher than the temperature measured in the experiment using  $N_2$  second positive bands emission spectra,  $T = 340 \pm 30$  K. However, it is well known that  $N_2$  second positive system emission decays over a few tens of nanoseconds after the discharge pulse. Note that temperature in the energy deposition region predicted at  $t = 40$  ns more reasonably matches the experiment, with a peak temperature of  $T = 410$  K. In addition, the average temperature along the stagnation line (within the shock layer) during the first 40 ns of the energy deposition pulse computation is  $T = 355$  K.

Confirmation of the post-shock temperature 50 nanoseconds after the discharge event suggests that the significant temperature rise seen later in the computation could actually be occurring in the experiment or that the strong temperature rise is merely an artifact of the phenomenological deposition modeling processing including the shape, distribution, and duration of the deposition. Verifying this requires taking additional temperature measurements during the experiment at much longer time delays after the discharge pulse ( $t = 1$   $\mu$ s), a challenge still being pursued, though the recent picosecond CARS results<sup>33</sup> may produce a method for obtaining the necessary measurements.

Figure 23(a) plots wall pressure coefficient distributions for several time delays after the energy deposition pulse. It can be seen that the initial pressure rise due to energy deposition is followed by a rarefaction wave. At  $t = 1.2$   $\mu$ s and  $2.0$   $\mu$ s, the rarefaction wave reduces the wall pressure coefficient below baseline value for the first  $15^\circ$  along the cylinder surface. The wall pressure perturbation is subsequently reduced and approaches baseline profile approximately at  $t = 4$   $\mu$ s, which has been excluded from figure as it overlaps the baseline solution.

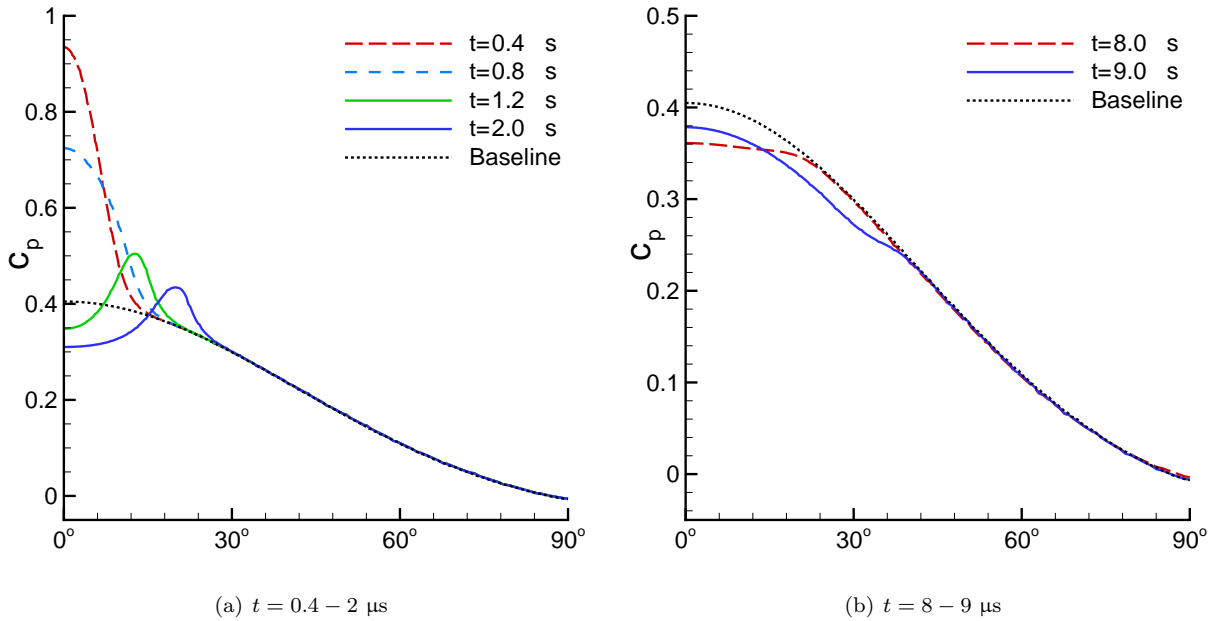
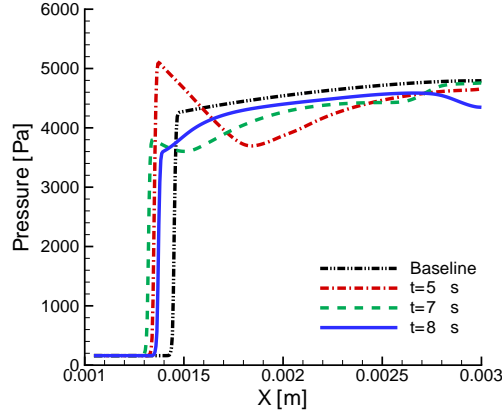


**Figure 23. Surface pressure coefficient for different time delays after beginning of energy deposition pulse**

Figure 23(b) shows wall pressure coefficient distributions at  $t = 8$   $\mu$ s and  $9$   $\mu$ s, displaying a second wall pressure ‘dip’ near the stagnation line. The second pressure reduction is due to a rarefaction wave, which reflects off the perturbed bow-shock and returns back to the cylinder. The movement of the rarefaction wave is also visible in Fig. 24, which plots pressure distributions along the stagnation streamline for different time delays after the pulse.

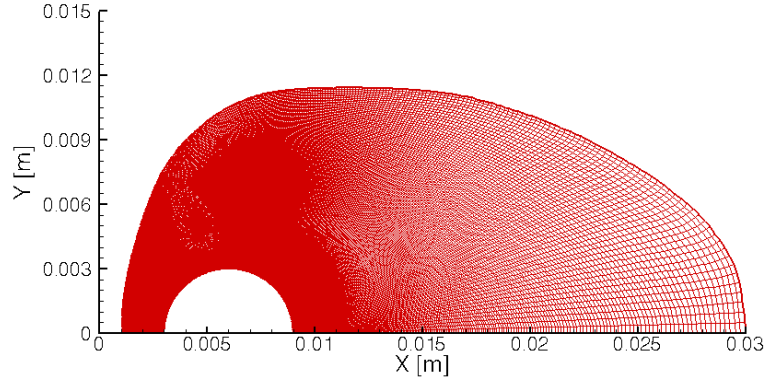
To determine the drag on the cylinder, the computational domain is extended to include the recirculating wake region, as shown in Fig. 25. The grid used for these calculations is  $401 \times 401$  points, with the grid resolution for  $0^\circ < \theta < 90^\circ$  being the same as the medium resolution grid discussed previously.

Figure 26(a) shows time evolution of total drag (i.e., the sum of pressure drag and shear drag over the



**Figure 24.** Pressure distributions along the stagnation streamline at  $t = 5 \mu\text{s}$ ,  $7 \mu\text{s}$ , and  $8 \mu\text{s}$  delays after the energy deposition pulse.

cylinder surface). The total drag for the baseline steady-state scenario is  $D = 2.4 \text{ N}$ . Note that shear drag accounts for 1% of the drag due to the low temperatures observed in the experiment. The drag reaches a maximum  $D = 3.04 \text{ N}$  (26% increase from the baseline), at  $t = 400 \text{ ns}$ , and a minimum  $D = 2.27 \text{ N}$  (5% decrease from the baseline) at  $t = 8.5 \mu\text{s}$ . Following the interaction with the rarefaction wave on the cylinder, the drag recovers the baseline value around  $t = 15 \mu\text{s}$  after the discharge event.



**Figure 25.** Computational domain used for drag calculations ( $401 \times 401$ ).

To evaluate the effect of energy deposition on drag reduction, the time-averaged change in total drag is shown in Fig. 26(b). As seen in the figure, the drag increases up to 20% at  $t = 1 \mu\text{s}$ , and then monotonically decreases to -1% at  $t = 11 \mu\text{s}$ , and remains unchanged thereafter. Figure 26(b) show that the nanosecond DBD discharge provides a slight reduction in total drag over the lifetime of the discharge event. However, the drag reduction comes with a substantial increase to the heat load on the cylinder.

To test if there is a continued reduction in drag by repetitive discharge events, three additional scenarios are considered. The first repeats the energy deposition at  $t = 15 \mu\text{s}$  (i.e, the discharge event begins after the previous discharge event cycle). This would be consistent with an operational frequency of 67 kHz. The results essentially replicate those previously presented for a single pulse effect, which suggests the 1% drag reduction on the cylinder could be sustained if the DBD was pulsed at this frequency. In the second scenario, the second discharge event begins when the total drag is at its lowest ( $t = 8.5 \mu\text{s}$  after the discharge event), which corresponds to an operational frequency of 110 kHz. The third scenario starts the second discharge event at  $t = 11 \mu\text{s}$ , which corresponds to the lowest time-averaged drag, or an operating frequency of 90 kHz.

Figure 27 shows the total drag time histories for repetitive discharges. As seen in the figure, neither of the higher frequency repetitive energy deposition scenarios resulted in an improvement to the total drag reduction. This occurs because the temperature in the energy deposition region is slightly hotter during

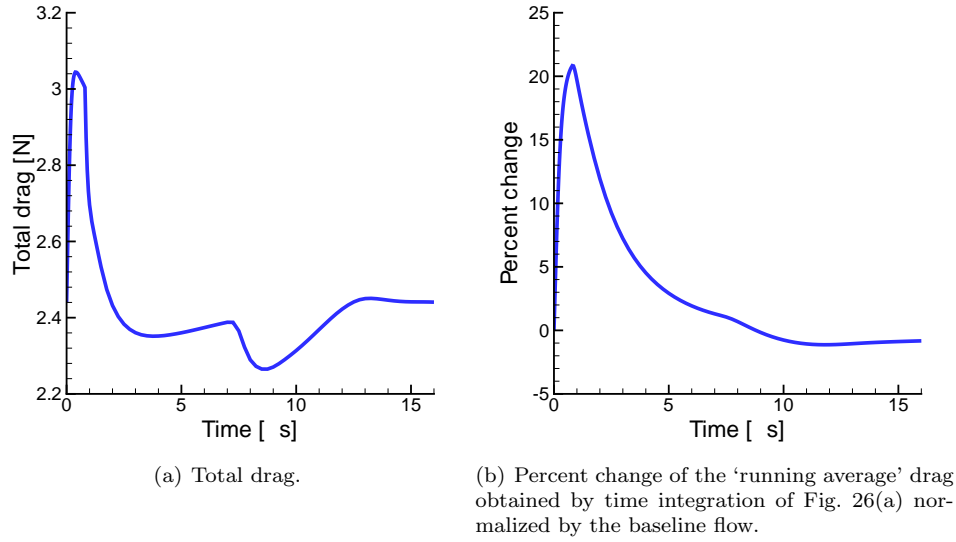


Figure 26. Time evolution of drag on the cylinder, calculated using the grid show in Fig. 25.

the second discharge (for the two higher frequency scenarios), since the flow has less time to cool down between discharge events. As a result, the energy deposited during the second pulse has a diminished effect in generating the subsequent compression wave, so its interaction with bow-shock is also reduced. These results suggest that it is best to operate the nanosecond DBD actuator at 67 kHz when it is being used for continuous operation since the total power requirements are the lowest, and it is still able to maintain the 1% reduction in running average total drag over the discharge cycle.

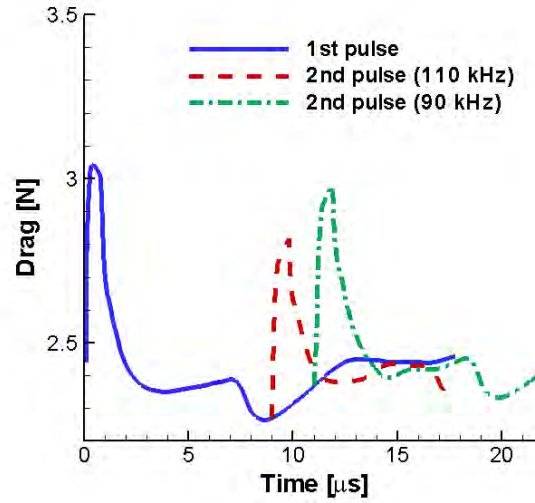
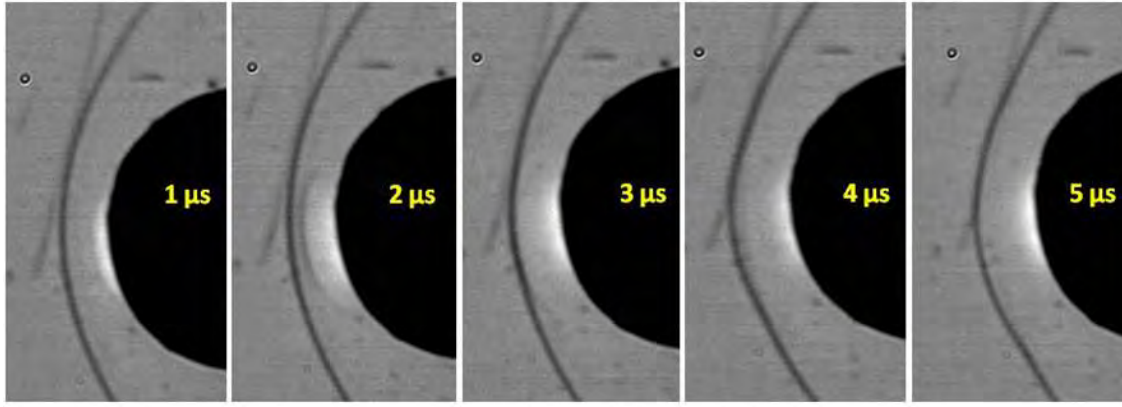


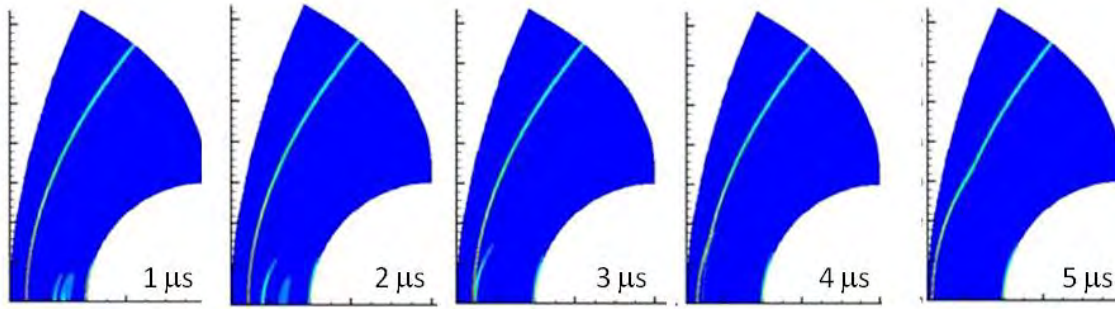
Figure 27. Time evolution of the total drag on the cylinder, with a second energy deposition pulse generated at  $t = 9\mu\text{s}$  (110 kHz) and  $t = 11\mu\text{s}$  (90 kHz).

As a final exploration using two-dimensional simulations, a simulation is performed with an input power  $Q = 35\text{ kW}$  over  $\tau = 200\text{ ns}$  (7 mJ/pulse for a whole cylinder, though the computation was performed using the  $1/4$  cylinder domain). This simulation was conducted in order to obtain a compression wave with sufficient speed such that the shock-shock interaction occurred in the same time as the experiment. In Fig. 28, simulation results are shown at the same time moments as the experimental phase-locked schlieren images. The figure shows many similarities between the bow-shock perturbation from the experiment and the computation.





(a) Phase-locked schlieren images



(b) CFD generated density gradient distributions

**Figure 28.** Temporal evolutions of the bow-shock (a) schlieren photography (experiment) and (b) density gradient distribution in the streamwise direction (CFD).

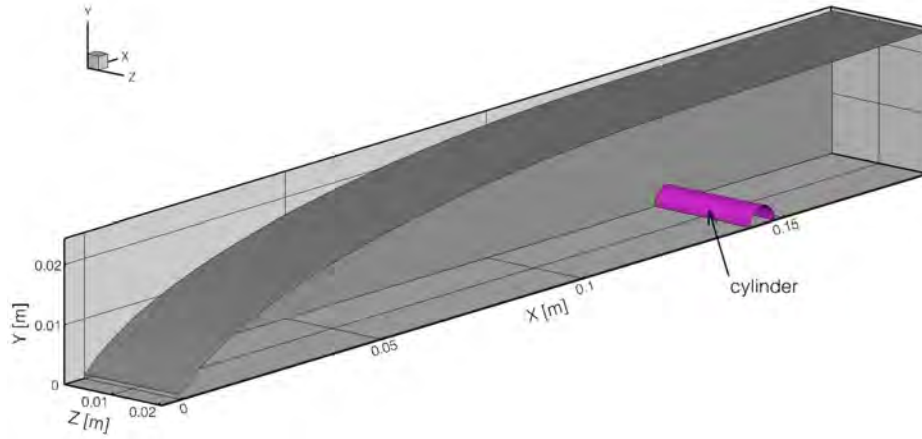
As seen in the Fig. 28, the generated compression wave propagates upstream and reaches the bow-shock at  $t = 3 \mu\text{s}$ . The interaction results in a 25% increase in the shock location from the baseline standoff distance, which is consistent with the results observed in the experiment's schlieren images. Note in this simulation, higher power input was required for the compression wave to reach the bow-shock at  $t = 3 \mu\text{s}$ , while compensating for a 30% difference in the bow-shock standoff distance. It would require a significantly smaller amount of deposition energy for a compression wave to travel 1.2 mm in the same amount of time.

## V. 3D Simulations

As previously discussed, the two-dimensional nominal baseline simulation predicts a bow-shock standoff distance that is significantly larger than that observed in the experiment. Several two-dimensional simulations were performed to quantify the uncertainty of the freestream and boundary conditions, along with thermochemical nonequilibrium flow effects. However, the results did not explain the observed discrepancy in shock location. As such, a simulation of the entire tunnel (including the nozzle and the region downstream of the test section), is performed in order to replicate the experiment's shock standoff distance and identify the reason for the discrepancy in bow-shock location. Details about the tunnel were previously mentioned in Section II. Note Fig. 29 provides an outline of the computational domain used in the simulation. Only  $1/4$  of the tunnel is simulated because the tunnel is assumed to be symmetric in both the spanwise and transverse directions. The nozzle throat conditions used in the simulation are listed in Table 5.

**Table 5.** Input conditions for the Mach 5 wind tunnel at the nozzle throat.

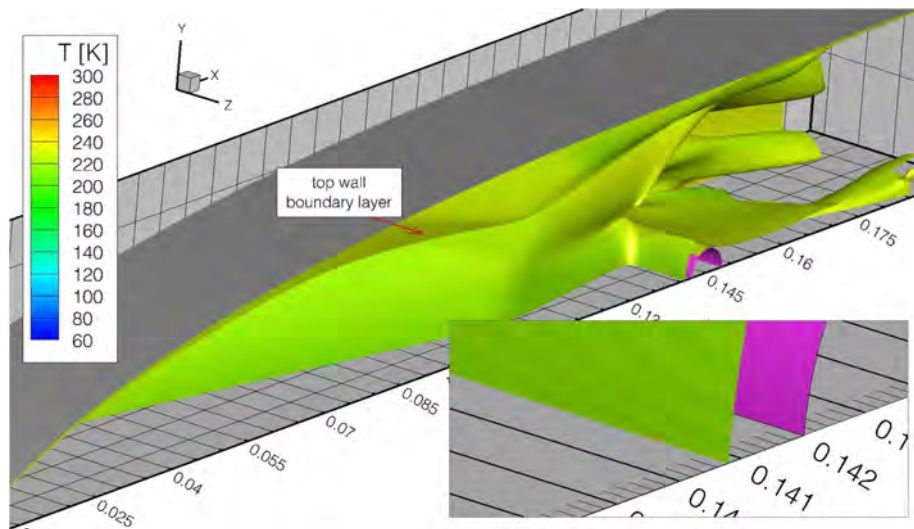
| Parameter                       | Value  |
|---------------------------------|--------|
| $u^*$ , [m/s]                   | 318    |
| $T^*$ , [K]                     | 250    |
| $\rho^*$ , [kg/m <sup>3</sup> ] | 0.3609 |
| $p^*$ , [Pa]                    | 26,020 |
| Mach*                           | 1.0    |



**Figure 29.** The computational domain for the entire tunnel. The gray surface depicts the tunnel while the pink surface illustrates the location of the cylinder test article. Only  $1/4$  of the geometry is simulated.

Using the lessons learned from the two-dimensional simulations, a grid was developed for the tunnel using 4 computational blocks. Each block is composed of structured cells. The grid spacing is such that grid clustering occurs near all surfaces. The computational block surrounding the cylinder geometry is identical to the grid-independent ‘medium’ grid used for the two-dimensional analysis. In total, the three-dimensional computational domain contains 15 M cells and was run using 512 processors. For the baseline simulation (i.e., without the discharge event), implicit time integration was employed with a time step-size varying from  $\Delta t = 0.1$  ns to  $\Delta t = 2$   $\mu$ s.

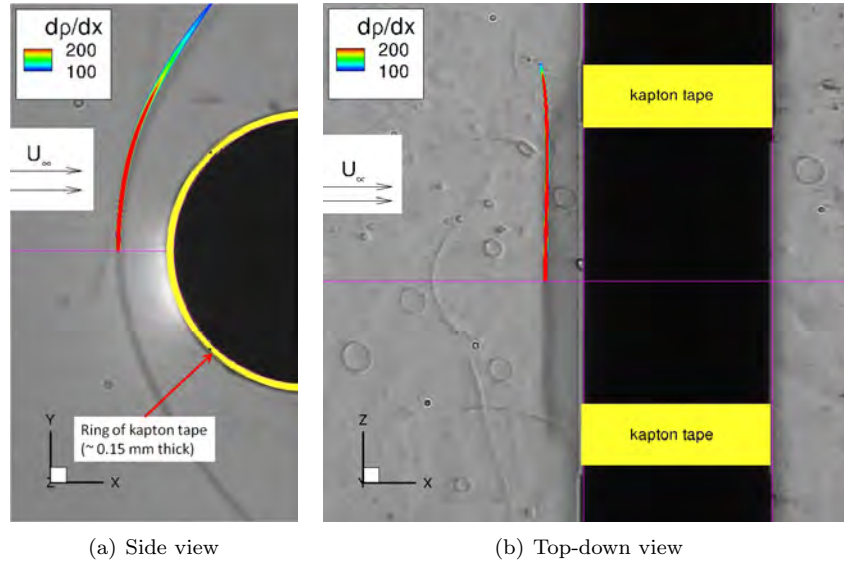
No slip, isothermal walls ( $T_w = 300$  K), are assumed for all surfaces and a non-reflective first-order extrapolation is used at the domain exit plane. The simulation is started from quiescent air, except for the input conditions listed in Table 5. As a result, the simulation required about 20 milliseconds ( $\sim 30,000$  iterations), for the wall boundary layer and cylinder bow-shock structure to develop and achieve a quasi steady-state in the inviscid region. Figure 30 shows a Mach 1.25 iso-surface of the flow, which is colored by temperature. This iso-surface level was selected as it illustrates the substantial growth of the sidewall boundary layer as the flow expands in the tunnel. It is also easy to see that the top wall boundary does not grow as dramatically due to the  $1.5^\circ$  divergence of the top wall. In addition, the figure shows the bow-shock standoff distance is 1.23 mm from the cylinder (as seen in the zoomed box), which matches the experiment’s measurement of the shock location.



**Figure 30.** Mach 1.25 iso-contour colored by temperature at  $t = 19$  ms. The pink surface indicates the cylinder for the  $1/4$  geometry simulation of air expanding in a Mach 5 wind tunnel.

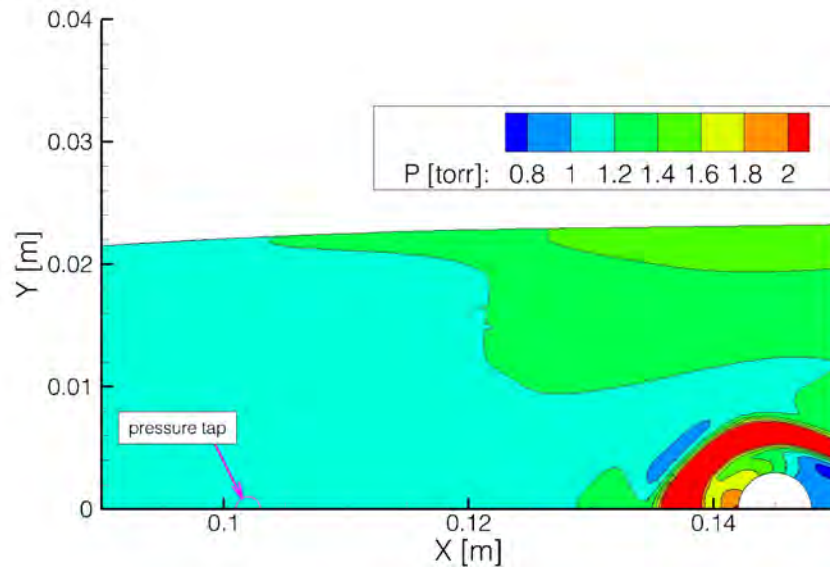


Figure 31 shows the phase-locked schlieren images from the experiment, which have been overlaid with the computational solutions. The schlieren images in the experiment were taken with a knife-edge set in the streamwise direction. To replicate this, the computational schlieren result is computed in the same direction (i.e., spanwise average of the derivative of density in the  $x$ -direction). Accounting for the thickness and location of the Kapton<sup>®</sup> tape placed on the cylinder, it can be seen that the computational shock standoff distance matches the experimental quite well.



**Figure 31.** Schlieren images from the experiment, along with the computational density gradient in the  $x$ -direction at  $t = 40$  ms.

Aside from schlieren visualization, the only other validation available from the experiment is the surface pressure tap located on sidewall of the tunnel, 4 cm upstream of the cylinder. Figure 32 plots the pressure on the tunnel sidewall. The computed pressure at the location of the pressure tap is  $p_w = 1.1$  Torr, which is slightly lower than the experimental value of  $p_w = 1.2$  Torr. However, given the precision of the experimental measurement ( $\pm 0.05$  Torr), and the uncertainties associated with the tunnel conditions, the computational results are consider to be in very good agreement with the experimental measurement.



**Figure 32.** Pressure contours along the sidewall the Mach 5 wind tunnel with a 6 mm cylinder in the test section. Flow direction is left to right. ( $t = 20$  ms)

In addition to the location of the bow-shock, Fig. 30 also illustrates the complexity of the flow-field, including a reflected Mach wave downstream of the cylinder wake along the flow spanwise centerline. In particular, the interaction between the cylinder and sidewall results in a complex wake region that oscillates at a low frequency (30 Hz). The low frequency oscillation of the boundary layer is due to interaction between the sidewall and the cylinder body, and is a characteristic of wall/blunt-body experiments, where a lambda shock structure forms at the edge of the inviscid region and the boundary layer. The oscillation in the wake region of the cylinder/side-wall interaction can be seen in Fig. 33, which shows the Mach 1.25 iso-surface, but viewed looking upstream. Oscillations at the shock/boundary layer junction were also observed in schlieren images from the experiment.

As seen in Fig. 34, the pressure is essentially uniform in the boundary layer, but rapidly changes in the inviscid region (decreasing when the Mach number is increasing and increasing where the Mach number is decreasing). As such, the assumptions made to originally estimate the tunnel's flow conditions were appropriate (i.e., constant static pressure through the boundary layer), but the approach did not account for the rapid increase in boundary layer thickness so far upstream of the test article. As a result, the inviscid flow just upstream of the cylinder's bow-shock is Mach 4 (rather than Mach 5). According to Billig's empirical formulation, the decrease in freestream Mach number should further increase the shock standoff distance, but due to the complex flow structures from the cylinder/side-wall junction, the bow-shock remains close to the geometry.

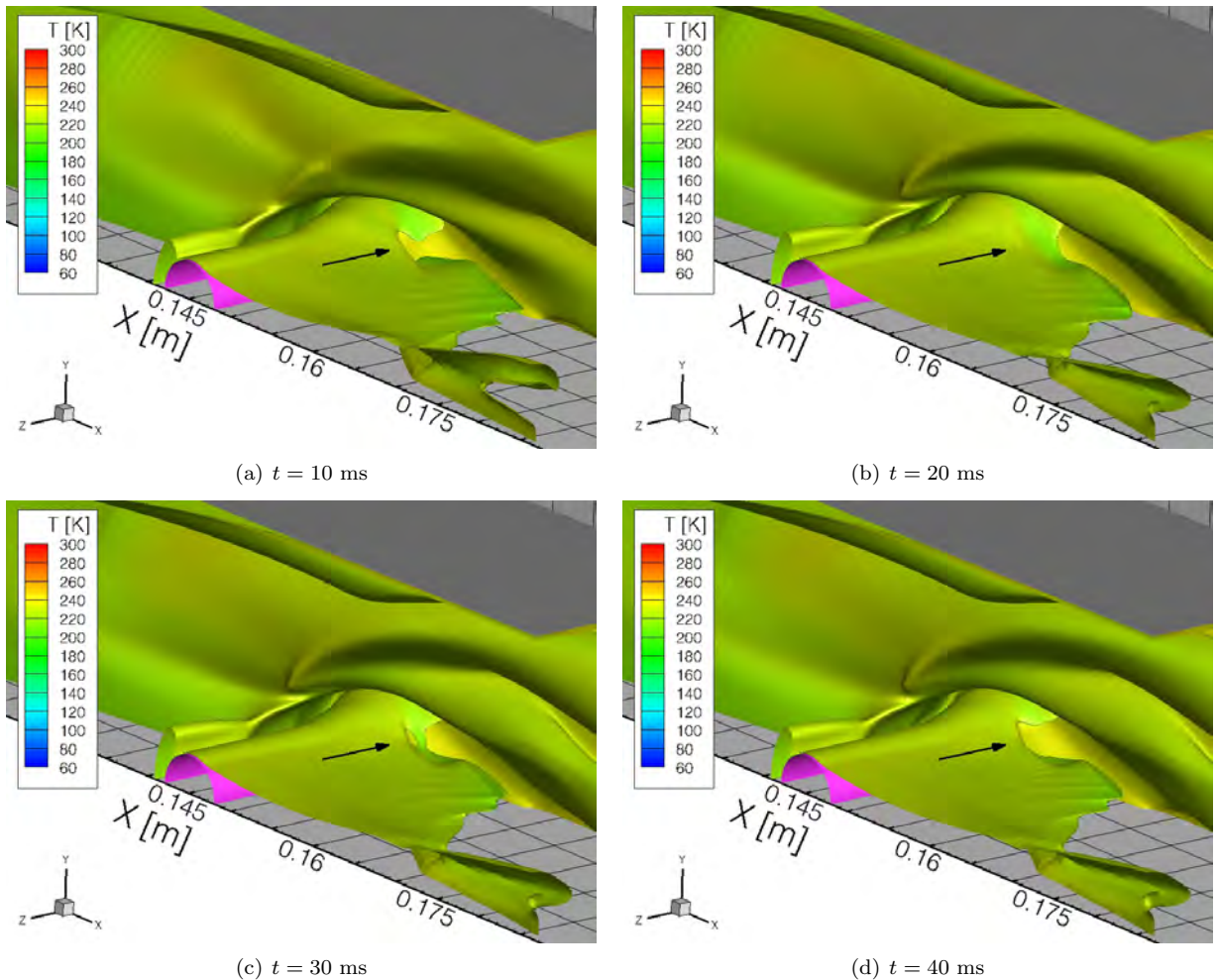


**Figure 33.** Mach 1.25 iso-surface colored by temperature for Mach 5 air in a wind tunnel. The cylinder/side-wall junction results in a complex wake flow that ‘breathes’ over a 30 ms cycle ( $\sim 30$  Hz).

As the flow accelerates through the nozzle, the pressure in the inviscid core drops, but due to the thick boundary layer far upstream of the test section, the inviscid core flow eventually contracts and slows slightly.

The decrease in Mach number coincides with an increase in static pressure within the inviscid core. As a result, there is a higher post bow-shock pressure and a larger spanwise pressure gradient in that region. Figure 34 shows Mach number and pressure contours along the transverse symmetry plane upstream of the test section.

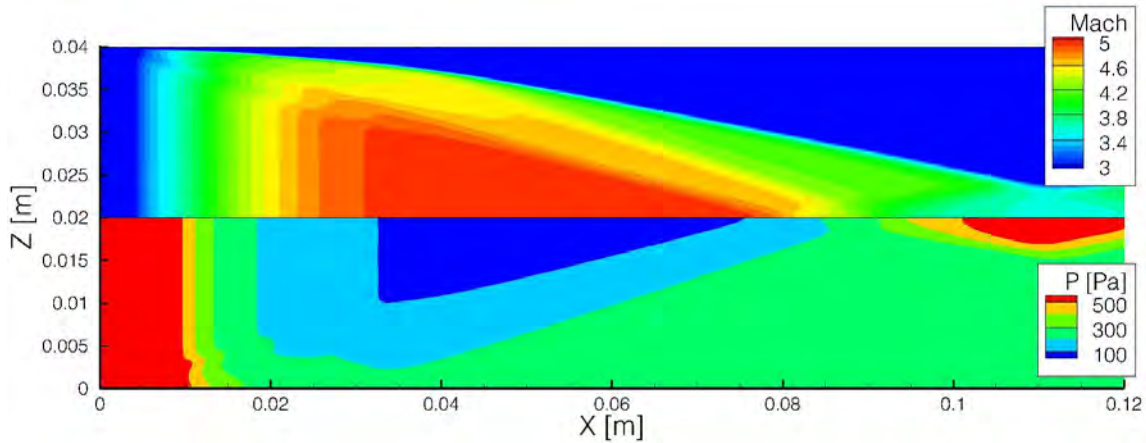


Figure 34. Top-down view of Mach and pressure contours along the transverse symmetry plane ( $y = 0$ ), for air flow in a Mach 5 wind tunnel.

Figure 35 shows a slice of pressure contours along the transverse symmetry plane near the cylinder. As seen in the figure, there is a very large pressure drop in the spanwise direction just after the bow-shock. This pressure drop is due to the low pressure present in the boundary layer, and is further strengthened due to the strong interaction between the cylinder with the sidewall.

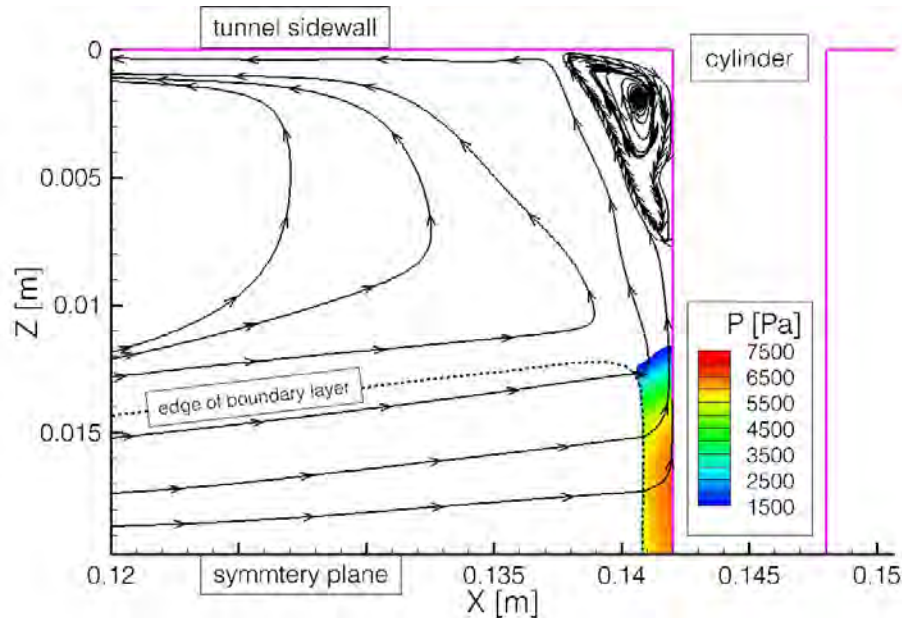


Figure 35. Top-down view of pressure contours along the transverse symmetry plane ( $y = 0$ ), for air flow in a Mach 5 wind tunnel. The figure also includes streamlines of velocity. Note contours  $p < 1500$  Pa have been excluded.

The large pressure gradient causes the inviscid core flow to turn into the spanwise direction after it goes through the bow-shock. While the post-shock flow escaping into the boundary layer is subsonic, it still has a large velocity and, as such, a large portion of the mass flow is no longer two-dimensional. As a result of the three-dimensionality of the flow, the bow-shock location is much closer to the cylinder than would be expected in a two-dimensional flow.

## A. Energy Deposition

Once the three-dimensional baseline simulation results were completed, a simulation of the discharge event was computed using the same phenomenological discharge model as the two-dimensional results, except the model was extended for three-dimensions:

$$S = \frac{Q}{\pi^{3/2} a b c} \exp \left( - \left( \frac{\hat{x}}{a} \right)^2 - \left( \frac{\hat{y}}{b} \right)^2 - \left( \frac{\hat{z}}{c} \right)^2 \right) \quad (7)$$

$$\begin{aligned} \hat{x} &= (x - x_c) \\ \hat{y} &= (y - y_c) \\ \hat{z} &= (z - z_c) \end{aligned}$$

where the center of the ellipsoid is set to the stagnation point of the cylinder along both symmetry planes (so half the ellipsoidal volume is inside the cylinder, and is excluded from the computational domain). For the wind tunnel geometry shown previously, the values are  $x = 14.2$  cm,  $y = 0$ ,  $z = 2.0$  cm. The equatorial radii of the ellipsoidal deposition are consistent with the two-dimensional simulations, and the polar radius,  $c$ , is half the width of the exposed electrode ( $a = 0.1$  mm,  $b = 0.3$  mm,  $c = 5$  mm). Note  $\iiint_{-\infty}^{\infty} S dx dy dz = Q$

The simulation was carried out assuming a total power deposition  $Q = 5$  kW for 100 ns (for  $1/4$  the geometry), at a time step of  $\Delta t = 0.5$  ns to ensure temporal independence based on the two-dimensional simulations. The power deposited amounts to a total energy deposition of 2 mJ/pulse, (i.e., a thermal efficiency of over 25%). While the computational representation of the discharge event results in a relatively high thermal efficiency, the value of  $Q$  was selected to ensure a supersonic compression wave was generated.

The simulation is run for 15  $\mu$ s using a  $\Delta t = 0.5$  ns time-step (i.e., 30,000 iterations) to capture the evolution of the compression wave/bow-shock interaction. Figure 36 shows the Mach 1.25 iso-surfaces colored by temperature at  $t = 4.1$   $\mu$ s after the deposition event.

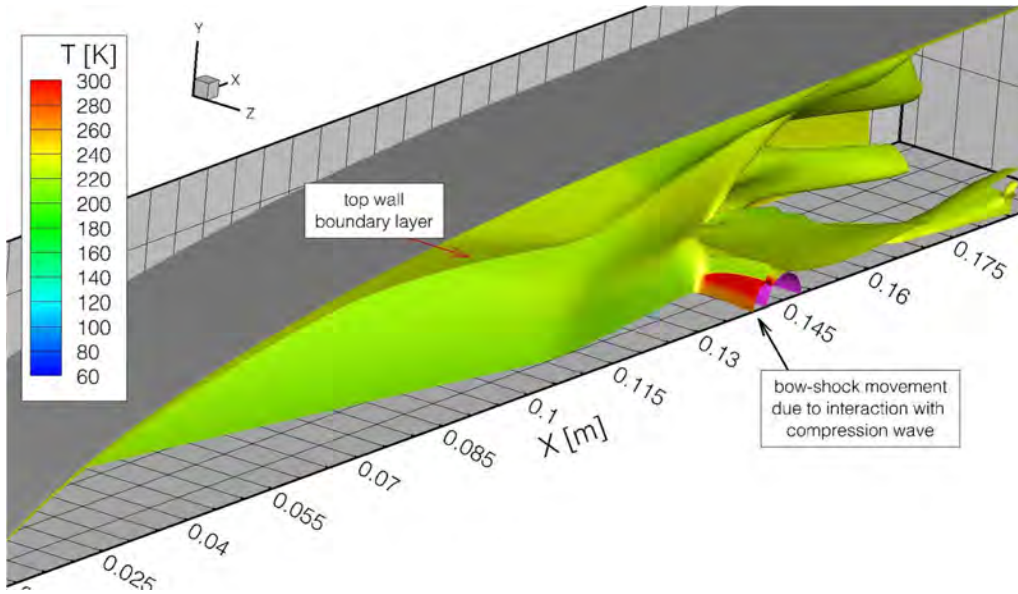


**Figure 36.** Mach 1.25 iso-contour colored by temperature for air in a Mach 5 wind tunnel  $t = 4.1$   $\mu$ s after a discharge event. The compression wave pushes the bow-shock outward, as seen in the red region.

Consistent with the two-dimensional results, the power deposited by the phenomenological model was sufficiently high to generate a supersonic compression, which traveled upstream and interacts with the standing bow-shock. However, either the energy was deposited over too small an area, and/or too much energy was deposited, because the compression wave speed was slightly faster than the experimental value and, thus, started interacting with the bow-shock before the time observed experimentally with the phase-locked schlieren images. Further evolution of the flow shows the resultant compression wave/bow-shock structure extending out more than 2.2 mm from the cylinder (along the centerline), which is a 85% increase in the shock standoff distance. This increase is much higher than that observed in the experiment (25%). In addition, the shape of the perturbed shock does not completely match the shape in schlieren images. These



results suggest that both the shape and amount of energy deposited in the phenomenological deposition model need to be adjusted in order to fully replicate the experiment using three-dimensional simulations.

The extra computations needed to fine tune the three-dimensional phenomenological energy deposition model are beyond the current resources dedicated for this work. Future studies will further refine the reduced-order model, though given the high computational cost associated with the three-dimensional simulations, it may be more feasible to experimentally explore the nanosecond DBD on a 5 mm diameter cylinder since the two-dimensional computations and two-dimensional empirical correlation are in much better agreement with the experiment.

While the three-dimensional computation results do not replicate the exact behavior observed in the experiment, the solutions do show that the compression wave's interaction with the bow-shock is directly responsible for the bow-shock movement and that the movement is not the result of a portion of the compression wave interacting with flow in the cylinder/side-wall junction, since the flow remains quasi-steady in that region during the entire 15  $\mu$ s discharge cycle.

## VI. Conclusions

A computational study of Mach 5 air flow around a 6 mm cylinder with a nanosecond DBD discharge was replicated using high-fidelity numerical simulations in order to better understand the resulting flow perturbation and the impact the discharge event has on the flow and the cylinder surface. The shock standoff distance for the 6 mm cylinder scenario was found to be 20% smaller in the experiments than the predictions of the empirical correlation and computations. However, the computed shock standoff distance for a 5 mm cylinder agreed well with the empirical correlation and experiment. In order to determine the cause of the shock location discrepancy, the tunnel's uncertainty in freestream conditions were estimated, and computations performed. The freestream differences resulted in a variation of the bow-shock standoff distance of about  $\pm 3\%$ . In addition, the effects due to wall boundary conditions, including partial slip walls, as well as thermo-chemical nonequilibrium were found to provide an insignificant change in the bow-shock location. Therefore, the observed discrepancy is attributed to the interaction at the junction of the cylinder and sidewall which results in a complex, quasi-steady boundary layer. This complex flow acts to lower the post-shock pressure thereby drawing the bow-shock closer to the cylinder. This was verified with a three-dimensional simulation of the entire wind tunnel, which was able to computationally replicate the bow-shock structure seen in the schlieren photography, predict the width of the tunnel's inviscid core, and match static pressure with the experiment's sidewall pressure tap.

The effect of the nanosecond pulse surface dielectric barrier discharge on a Mach 5 flow over a cylinder model was modeled using two-dimensional compressible Navier-Stokes flow code, LeMANS, which incorporated a phenomenological thermal energy deposition model. In spite of a difference between the baseline bow-shock standoff distance measured in the experiments and that predicted by the CFD model, other experimentally measured parameters such as compression wave speed and perturbed bow-shock speed, as well as the time evolution of the perturbed bow-shock shape were replicated using the model. Distributions of wall pressure and heat transfer coefficient, as well as total drag on the model have also been calculated and show that the cylinder experiences a small reduction in total drag (1%), over a discharge event cycle of 15  $\mu$ s, though the cylinder is subjected to a large increase in peak heating during the first microsecond of the discharge cycle.

A three-dimensional simulation was also computed to replicate the discharge event from the baseline flow conditions. While these results do not agree as well with the experiment's phase-locked schlieren images as the two-dimensional results, the resultant flow field indicates that the cylinder/sidewall junction is not immediately influenced by the discharge event and therefore is not responsible for the increase in bow-shock standoff distance due to the nanosecond DBD pulse. In addition, the behavior of the shock perturbation is independent of the form of energy input (due to the short pulse duration), so the resultant flow is being accurately simulated.

While the nanosecond DBD actuator simulated in this work is not very effective at improving the cylinder surface conditions (i.e., it creates a large increase in heat load on the cylinder surface with only a minor decrease to total drag), the device is very effective at moving a strong standing shock. This technology could prove very useful in supersonic inlets and isolators found in RAM jet and SCRAM jet engines, where engine 'un-start' continues to be a technical challenge. One example of engine 'un-start' is the upstream movement of the shock-train within the inlet which leads to unfavorable conditions in the combustor. If 'un-start' of

the shock-train could be sensed in the inlet, a nanosecond DBD device could be rapidly fired to move the shock-train back to its nominal location.

From this work, it appears these devices would be best situated in subsonic regions of the flow (i.e., in the sub-sonic region of a separation bubble or in the subsonic region downstream of a bow-shock), where a supersonic compression wave could more easily be generated. Figure 37 illustrates the concept of placing a nanosecond DBD actuator at the leading edge of a supersonic inlet flow-path. As seen in the figure, the DBD induced bow-shock perturbation travels along the standing shock, effectively moving the subsequent shock-train.

This concept already has received some attention. In 2008, Gnemmi *et al.* successfully applied the concept of shock perturbation on external flows by using a short duration arc discharge,<sup>34</sup> as seen in Fig. 38. In their work, the surface discharge created a shock-wave perturbation on one side of a cone, which was used to generate a steering moment. Future work may explore using nanosecond DBD discharges for an internal flow-path to achieve similar shock control.

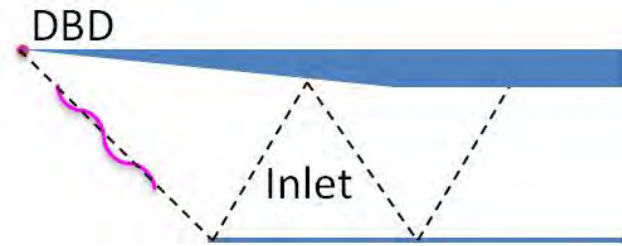


**Figure 37. Schematic illustrating a shock train perturbation due to nanosecond DBD actuator locating at the leading edge of a supersonic inlet.**

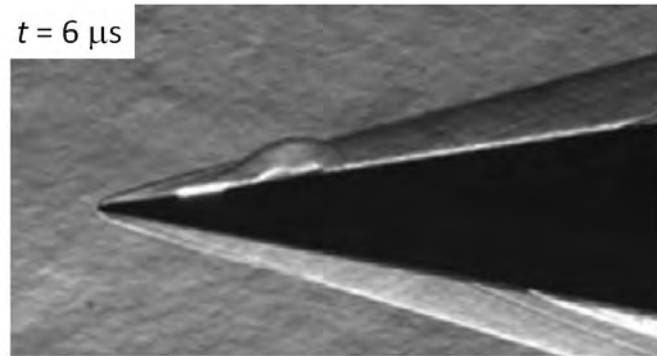


**Figure 38. Evolution of arc-discharge generated disturbance on the surface of a supersonic cone, taken from Ref. 34.**

In addition to exploration of the controlling shock boundary-layer interactions using nanosecond DBD actuators for internal flow paths, it is also necessary to improve the fidelity of the phenomenological energy deposition model. To this end, future work will incorporate the recent work by Poggie *et al.*,<sup>16</sup> which more accurately models the energy transfer processes in a pulsed surface dielectric barrier discharge.

## Acknowledgments

The authors would like to thank the Department of Defense High Performance Computing Modernization Program, the US Air Force Research Laboratory (AFRL DSRC), and the US Army Engineer Research and Development Center (ERDC DSRC), for the computation resources needed to conduct this study. The authors would also like to thank Prof. Iain Boyd for allowing the use of his CFD code, LeMANS and Dr. Jon Burt for his DSMC simulation results included in this study. This project is sponsored in part by the Air Force Office of Scientific Research (monitored by F. Fahroo). Work by The Ohio State University has been funded in part by the Chief Scientist Innovative Research Fund (CSIRF) of the Air Force Research Laboratory Air Vehicles Directorate AFRL/RB). This work is cleared for public release, distribution unlimited (88AFB-2011-6361).

## References

- <sup>1</sup>Nishihara, M., Takashima, K., Rich, J. W., and Adamovich, I. V., "Mach 5 Bow Shock Control by a Nanosecond Pulse Surface Dielectric Barrier Discharge," *Physics of Fluids*, Vol. 23, No. 6, 2011, pp. 066101.
- <sup>2</sup>Roupassov, D. V., Nikipelov, A. A., Nudnova, M. M., and Starikovskii, A. Y., "Flow Separation Control by Plasma

- Actuator with Nanosecond Pulsed-Periodic Discharge," *AIAA Journal*, Vol. 47, No. 1, January 2009, pp. 168–185.
- <sup>3</sup>Takashima, K., Zuzek, Y., Lempert, W. R., and Adamovich, I. V., "Characterization of a surface dielectric barrier discharge plasma sustained by repetitive nanosecond pulses," *Plasma Sources Science and Technology*, Vol. 20, No. 5, 2011, pp. 055009.
- <sup>4</sup>Little, J., Takashima, K., Nishihara, M., Adamovich, I., and Samimy, M., "High Lift Airfoil Leading Edge Separation Control with Nanosecond Pulse Driven DBD Plasma Actuators," AIAA Paper 2010-4256, 2010, submitted for publication in AIAA Journal.
- <sup>5</sup>Samimy, M., Adamovich, I., Webb, B., Kastner, J., Hileman, J., Keshav, S., and Palm, P., "Development and Characterization of Plasma Actuators for High Speed Jet Control," *Experiments in Fluids*, Vol. 37, No. 4, March 2004, pp. 577–588.
- <sup>6</sup>Utkin, Y. G., Keshav, S., Kim, J.-H., Kastner, J., Adamovich, I. V., and Samimy, M., "Development and use of localized arc filament plasma actuators for high-speed flow control," *Journal of Physics D*, Vol. 40, No. 3, February 2007, pp. 685–695.
- <sup>7</sup>Adamovich, I. V., Choi, I., Jiang, N., Kim, J.-H., Keshav, S., Lempert, W., Mintusov, E., Nishihara, M., Samimy, M., and Uddi, M., "Plasma Assisted Ignition and High-Speed Flow Control: Non-Thermal and Thermal Effects," *Plasma Sources Science and Technology*, Vol. 18, No. 3, 2009, pp. 034018.
- <sup>8</sup>Myrabo, L. N., Raizer, Y. P., Schneider, M. N., and Bracken, R., "Reduction of Drag and Energy Consumption during Energy Release Preceding a Blunt Body in Supersonic Flow," *High Temperature*, Vol. 42, No. 6, 2004, pp. 901–910.
- <sup>9</sup>Lashkov, V., Mashek, I., Anisimov, Y., Ivanov, V., Kolesnichenko, Y., Ryvkin, M., and Gorynya, A., "Gas Dynamic Effect of Microwave Energy Discharge on Supersonic Cone Shaped Bodies," AIAA Paper 2004-0671, 2004.
- <sup>10</sup>Adelgren, R. G., Yan, H., Elliott, G. S., Knight, D. D., Beutner, T. J., and Zheltovodov, A. A., "Control of Edney IV Interaction by Pulsed Laser Energy Deposition," *AIAA Journal*, Vol. 43, No. 2, 2005, pp. 256–269.
- <sup>11</sup>Sasoh, A., Sekiya, Y., Sakai, T., Kim, J.-H., and Matsuda, A., "Supersonic Drag Reduction with Repetitive Laser Pulses Through a Blunt Body," *AIAA Journal*, Vol. 48, No. 12, December 2010, pp. 2811–2817.
- <sup>12</sup>Bisek, N. J., Boyd, I. D., and Poggie, J., "Numerical Study of Plasma-Assisted Aerodynamic Control for Hypersonic Vehicles," *Journal of Spacecraft and Rockets*, Vol. 46, No. 3, May-June 2009.
- <sup>13</sup>Bisek, N. J., Boyd, I. D., and Poggie, J., "Numerical Study of Magnetoaerodynamic Flow Around a Hemisphere," *Journal of Spacecraft and Rockets*, Vol. 47, No. 5, September-October 2010.
- <sup>14</sup>Scalabrin, L. C. and Boyd, I. D., "Development of an Unstructured Navier-Stokes Solver For Hypersonic Nonequilibrium Aerothermodynamics," AIAA Paper 2005-5203, 2005.
- <sup>15</sup>Scalabrin, L. C. and Boyd, I. D., "Numerical Simulation of Weakly Ionized Hypersonic Flow for Reentry Configurations," AIAA Paper 2006-3773, 2006.
- <sup>16</sup>Poggie, J., Bisek, N. J., Adamovich, I., and Nishihara, M., "High-Speed Flow Control with Nanosecond-Pulse Electrical Discharges," AIAA Paper, January 2012, submitted to the AIAA Aerospace Sciences Meeting, 2012.
- <sup>17</sup>Nishihara, M., Takashima, K., Jiang, N., Lempert, W., Adamovich, I. V., and Rich, J. W., "Development of a Mach 5 Nonequilibrium Wind Tunnel," AIAA Paper 2010-1567, 2010.
- <sup>18</sup>Nishihara, M., Takashima, K., Jiang, N., Lempert, W., Adamovich, I. V., and Rich, J. W., "Nonequilibrium Flow Characterization in a Mach 5 Wind Tunnel," AIAA Paper 2010-4515, 2010.
- <sup>19</sup>Jiang, N., Nishihara, M., and Lempert, W. R., "Quantitative NO<sub>2</sub> Molecular Tagging Velocimetry at 500 kHz Frame Rate," *Applied Physics Letters*, Vol. 97, No. 22, 2010, pp. 221103.
- <sup>20</sup>Montello, A., Nishihara, M., Rich, J. W., Adamovich, I. V., and Lempert, W., "Picosecond CARS Measurements of Vibrational Distribution Functions in a Nonequilibrium Mach 5 Flow," AIAA Paper 2011-1322, 2011.
- <sup>21</sup>Jiang, N., Webster, M., and Lempert, W. R., "New Advances in Generation of High Repetition Rate Burst Mode Laser Output," *Applied Optics*, Vol. 48, No. 4, 2009, pp. B23–B31.
- <sup>22</sup>Popov, N., "Investigation of the Mechanism for Rapid Heating of Nitrogen and Air in Gas Discharges," *Plasma Physics Reports*, Vol. 27, No. 10, 2001, pp. 886–896.
- <sup>23</sup>Ambrosio, A. and Wortman, A., "Stagnation Point Shock Detachment Distance for Flow Around Spheres and Cylinders," *ARS Journal*, Vol. 33, No. 2, 1962, pp. 281.
- <sup>24</sup>Billig, F. S., "Shock-Wave Shapes around Spherical- and Cylindrical-Nosed Bodies," *Journal of Spacecraft*, Vol. 4, No. 6, 1967.
- <sup>25</sup>White, F. M., *Heat Transfer*, 1984, Addison-Wesley Publishing Company.
- <sup>26</sup>Marks, L. S., *Mechanical Engineers Handbook*, 1941, McGraw-Hill Book Company.
- <sup>27</sup>23. Vincenti, W. G. and Kruger, C. H., *Introduction to Physical Gas Dynamics*, 2002, Krieger Publishing Company.
- <sup>28</sup>Gordiets, B. and Ricard, A., "Production of N, O and NO in N<sub>2</sub>-O<sub>2</sub> flowing discharges," *Plasma Sources Science and Technology*, Vol. 2, No. 3, 1993, pp. 158–163.
- <sup>29</sup>Boyd, I. D., Chen, G., and Candler, G. V., "Predicting Failure of the Continuum Fluid Equations in Transitional Hypersonic Flows," *Physics of Fluids*, Vol. 7, No. 1, 1995.
- <sup>30</sup>Lofthouse, A., *Nonequilibrium Hypersonic Aerothermodynamics Using the Direct Simulation Monte Carlo and Navier-Stokes Models*, 2008, PhD thesis, Department of Aerospace Engineering, University of Michigan.
- <sup>31</sup>Lockerby, D. A., Reese, J. M., Emerson, D. R., and Barber, R. W., "Velocity Boundary Conditions at Solid Walls in Rarefied Gas Calculations," *Physical Review E*, Vol. 70, 2004, pp. 017303.
- <sup>32</sup>Burt, J. M., Josyula, E., and Boyd, I. D., "A Novel Cartesian Implementation of the Direct Simulation Monte Carlo Method," AIAA Paper 2011-632, 2011.
- <sup>33</sup>Montello, A., Nishihara, M., Rich, J., Adamovich, I., and Lempert, W., "Unstable-Resonator Spatially Enhanced Detection Picosecond CARS Measurements of Vibrational Distribution Functions in and Around a Bow Shock in a Highly Nonequilibrium Mach 5 Flow," AIAA Paper, January 2012, submitted to the AIAA Aerospace Sciences Meeting, 2012.
- <sup>34</sup>Gnemmi, P., Charon, R., Duperoux, J.-P., and A., G., "Feasibility Study for Steering a Supersonic Projectile by a Plasma Actuator," *AIAA Journal*, Vol. 46, No. 6, June 2008, pp. 1308–1317.